ChemPubSoc Europe

DOI: 10.1002/chem.201705267

CHEMISTRY A European Journal Full Paper

Medical Chemistry

Benzothiazole-Based Cycloplatinated Chromophores: Synthetic, Optical, and Biological Studies

Elena Lalinde,*[a] Rebeca Lara,[a] Icíar P. López,[b] M. Teresa Moreno,*[a] Elvira Alfaro-Arnedo,[b] José G. Pichel,*[b] and Sergio Piñeiro-Hermida[b]

Dedicated to Professor Peter Maitlis on the occasion of his 85th birthday

Abstract: Cycloplatinated complexes based on 2-(4-substituted)benzothiazole ligands of type [Pt(R-PBT-κ*C*,*N*)Cl(L)] (PBT = 2-phenylbenzothiazole; R = Br (**1**), Me_2N (**2**); L = dimethyl sulfoxide (DMSO; **a**), 1,3,5- triaza-7-phosphaadamantane (PTA; **b**), triphenylphosphine 3,3′,3′′-trisulfonate (TPPTS; **c**)) and [Pt(Br-PBT-κ*C*)Cl$(PTA)_2$] (**3**) are presented. On the basis of the photophysical data and time-dependent (TD)-DFT calculations (**1a** and **2a**), the low-lying transitions (absorption and emission) were associated with ligand-center (LC) charge transfer, with minor metal-to-ligand charge transfer (MLCT), and intraligand charge transfer (ILCT) [Me_2N-PBT→PBT] excited states, respectively. Simultaneous fluorescence/phosphorescence bands were found in fluid solutions (and also in the solid state for **2a**), which become dominated by triplet emission bands in rigid media at 77 K. The effect of the concentration on emissive behavior of **2a**,**b** indicated the occurrence of aggregation-induced luminescence properties related to the occurrence of metal–metal and π···π interactions, which are more enhanced in **2a** because of the less bulky DMSO ligand. The behavior of **2a** toward *para*-toluenesulfonic acid (PTSA) in aerated acetonitrile and to hydrogen chloride gas in the solid state has been evaluated, thus showing a clear reversible change between the ^{1}ILCT and ^{3}LC/^{3}MLCT states due to protonation of the NMe_2 group (theoretical calculations on **2a-H$^+$**). Solid **2a** undergoes a surprising oxidation of the Pt^{II} center to Pt^{IV} with concomitant deoxygenation of DMSO, under prolonged reaction with hydrogen chloride gas to afford the Pt^{IV}/dimethyl sulfide complex (*mer*-[Pt(Me_2N-PBT-κ*C*,*N*)$Cl_3(SMe_2)$]; ***mer*-4**), which evolves in solution to ***fac*-4**, as confirmed by X-ray studies. Cytotoxic activity studies on A549 and HeLa cell lines indicated cytotoxic activity of **1b** and **2a**,**b**. In addition, fluorescent cell microscopy revealed cytoplasmic staining, more visible in perinuclear areas. Inhibition of tubulin polymerization by **1b** in both cells is presented as a preliminary mechanism of its cytotoxic action.

Introduction

In the last few decades, phosphorescent cyclometalated complexes of heavy transition metals have received great attention because of their rich physicochemical properties, such as high photo- and electrochemical stability, high photoluminescence quantum yield, tunable emission color, and long-lived emissive excited state, with a wide range of potential applications in many areas.[1] A fascinating research field is currently represented by the use of these complexes in medicine and bioimaging[2] because they are generally rather stable due to the presence of σ(M–C) bonds, which allow the organometallic fragment to reach the cell unaltered, and their properties can be easily tuned by modification of either the anionic cyclometalated or the ancillary ligands, thus varying their cytotoxicity and pharmacokinetics. In particular, although the number of studies of anticancer activity of cycloplatinated complexes is significant,[2a,k,l,3] little is known about their mechanisms of action. These coordination compounds can be described as dual-function complexes;[4] that is, the presence of aromatic groups in the cyclometalated ligand might favor intercalative binding to DNA (π–π stacking),[2a,5] targeting the human telomeric G-quadruplex[2a,6] or key proteins,[2a,7] whereas labile positions in the coordination sphere may favor covalent coordination to DNA purine bases, as in cisplatin.[8,9]

On the other hand, the study of benzothiazole derivatives is presently of considerable interest due to their interesting biological and biophysical properties. 2-Aryl or 2-heteroaryl-substituted benzothiazoles have been studied in medicinal chemistry as antitumor,[10] antimicrobial,[11] and antifungal agents[12] as well as imaging agents for β-amyloid[13] or in the study of cellular processing of anticancer activity.[14] A series of potent and selective antitumor agents derived from 2-(4-aminophenyl)-

[a] *Prof. Dr. E. Lalinde, R. Lara, Dr. M. T. Moreno*
Departamento de Química-Centro de Síntesis Química de La Rioja (CISQ)
Universidad de La Rioja, 26006, Logroño (Spain)
E-mail: elena.lalinde@unirioja.es
teresa.moreno@unirioja.es

[b] *Dr. I. P. López, E. Alfaro-Arnedo, Dr. J. G. Pichel, S. Piñeiro-Hermida*
Lung Cancer and Respiratory Diseases Unit, Centro de Investigación Biomédica de La Rioja (CIBIR)
Fundación Rioja Salud, 26006, Logroño (Spain)
E-mail: jgpichel@riojasalud.es

Supporting information for this article can be found under: https://doi.org/10.1002/chem.201705267.

benzothiazole has been extensively developed,[10c] and even the fluorinated analogue, 2-(4-amino-3-methylphenyl)-5-fluorobenzothiazole, in the form of the L-lysylamide prodrug Phortess, entered a clinical phase I trial in 2002.[15] Due to the low toxicity, high bioavailability, and good biocompatibility of benzothiazole-based anticancer complexes, considerable work has been directed toward the development of these complexes with the ability to target different receptors, such as topoisomerases, microtubule, kinases, DNA, and so forth.[10f] Recently, the in vitro cytotoxic activity of the monofunctional $[Pt(BPA)Cl]^+$ (BPA = *N*,*N*-bis(pirydin-2-ylmethyl)amine)[14a] and two dichloride $[PtLCl_2]$ (L = 2-(4′aminophenyl)benzothiazole)[10b] platinum(II) complexes featuring benzothiazole-based pharmacophores were reported. However, although several cyclometalated Pt^{II} complexes based on 2-phenylbenzothiazole (PBT) are known,[16] as far as we know, no studies have been reported on their biological activity, except the recent report by our group concerning the neutral pentafluorophenyl complex $[Pt(PBT)(C_6F_5)(dmso)]$.[17]

Following our interest in platinum complexes containing chromophoric benzothiazole units,[17,18] we aimed to prepare a family of cyclometalated Pt^{II} complexes derived from 2-(4-substituted-phenyl)benzothiazoles 2-(4-bromophenyl)benzothiazole (Br-HPBT) and 2-(4-dimethylaminophenyl)benzothiazole (Me_2N-HPBT), respectively. Herein, we present the synthesis of cycloplatinated [Pt(C^N)ClL] systems **1** and **2** that contain chloride as a labile ligand and dimethyl sulfoxide (DMSO) and water-soluble phosphines, such as 1,3,5- triaza-7-phosphaadamantane (PTA) and triphenylphosphine 3,3′,3′′-trisulfonate ($P(C_6H_4SO_3Na)_3$; TPPTS) as auxiliary groups. These systems were designed by taking into account several features that make the complexes interesting for biological studies: 1) the planarity and presence of sulfur donor atoms on the cyclometalated benzothiazole ligand would favor DNA intercalative binding through noncovalent π-stacking interactions; 2) the presence of the NMe_2 substituent on the benzothiazole unit might make the complexes active in acidic media, such as the cytoplasm of cancer cells; 3) the chloride ligand could be easily substituted by interaction with DNA bases;[8,9] and, finally, 4) the non-leaving phosphine ligands (PTA and TPPTS) could enhance the solubility of the systems in biological media. In fact, use of these phosphines were recently explored as a co-ligand in several antineoplastic Ru^{II},[19] Pt^{II}, [20] and Au^{I} [21] complexes. A detailed study of the optical properties of these systems, with a particular emphasis on the interaction of complex [Pt(Me_2N-PBT)Cl(dmso)] (**2a**) with acids (i.e., $HSO_3C_6H_4CH_3$ and HCl), which was interpreted with the help of theoretical calculations, is presented. The interaction of **2a** with excess hydrogen chloride gas leads to an unexpected oxidation of the platinum center to Pt^{IV} with simultaneous deoxygenation of DMSO and the formation of *mer*-[Pt(Me_2N-PBT)$Cl_3(SMe_2)$] (***mer*-4**), which evolves in solution to ***fac*-4**. We have examined the antitumor activity of **1** and **2** against the human cancer-cell lines A549 (lung cancer) and Hela (cervix cancer) and evaluated a plausible mechanism of action of these complexes on the polymerization of microtubules. The compounds were also tested in vitro with confocal microscopy as labels for bioimaging.

Results and Discussion

Synthesis and characterization

Scheme 1 shows the method for the preparation of compounds **1a**–**c**, **2a**–**c**, and **3** and the numbering of the hydrogen and carbon atoms of the 2-(4-*R*-phenyl)benzothiazole ligands. The cyclometalation of Br-HPBT and Me_2N-HPBT was carried out by following a conventional protocol[22] to obtain cyclometalated Pt^{II}/μ-chloro-bridged complexes $[\{Pt(C^N)(\mu\text{-}Cl)\}_2]$, which involved heating $[\{Pt(\mu\text{-}Cl)(\eta^3\text{-}2\text{-}MeC_3H_4)\}_2]$[23] ($\eta^3$-2-$MeC_3H_4$ = η^3-2-methylallyl) to reflux with two equivalents of Br-HPBT or Me_2N-HPBT in toluene for 24 or 4 h, respectively. The treatment of the sparingly soluble dimers $[\{Pt(R\text{-}PBT)(\mu\text{-}Cl)\}_2]$ (R = Br, Me_2N) with dimethyl sulfoxide (DMSO) for 5 min at reflux, followed by evaporation and precipitation with isopropyl alcohol, gave the DMSO-coordinated compounds [Pt(R-PBT)Cl(DMSO)] (R = Br (**1a**), Me_2N (**2a**)). The phosphine derivatives [Pt(R-PBT)Cl(L)] (L = PTA, R = Br (**1b**), Me_2N (**2b**); L = TPPTS, R = Br (**1c**), Me_2N (**2c**)) were prepared by reaction of the corresponding DMSO complex **1a** or **2a** with one equivalent of the corresponding phosphine ligand. The presence of the negatively charged phosphine ligand made the TPPTS complexes highly soluble in polar media (i.e., D_2O, MeOD, and DMSO) and insoluble in $CDCl_3$ as a difference to the corresponding PTA derivatives. The spectroscopic data discussed below indicate that only the *trans*-C,Cl isomer is present in each case, as was previously found in related compounds.[22b,24] Complex [Pt(Br-PBT-κ*C*)Cl$(PTA)_2$] (**3**) was produced during an attempted synthesis of complex **1b** by reaction of $[\{Pt(Br\text{-}PBT\text{-}\kappa C,N)(\mu\text{-}Cl)\}_2]$ with PTA (molar ratio 1:3). A control reaction of the monophosphine complex **1b** with one additional equivalent of PTA in $CDCl_3$ reveals that the formation of **3**, which requires the N-dissociation of the hemilabile cyclometalated Br-PBT-κ*C*,*N* ligand in the presence of excess PTA ligand, takes places quantitatively and immediately (see Figure S1 in the Supporting Information), which was confirmed by X-ray studies (see below). N-dissociation of C^N ligands to give monocoordinated κ-*C* ligands is not a common occurrence, but has been observed in reactions of some C,*N*-cycloplatinated complexes.[24,25]

Complexes **1**–**3** were characterized (i.e., IR, NMR, MS, and elemental analysis and, in the case of **1a**,**b**, **2a**,**b**, and **3**, by X-ray diffraction studies; see the Experimental Section in the Supporting Information). Notably, the characteristic and more-deshielded proton of the C^N ligand (H^7) appears in the cyclometalated complexes downfield relative to the corresponding free ligand (δ = 9.65, 9.69, and 9.19 in **1a**–**c**, respectively, vs. 8.07 ppm in Br-PBT); δ = 9.47, 9.54, and 9.54 in **2a**–**c**, respectively, vs. 8.04 ppm in Me_2N-PBT), whereas the proton adjacent to the metalated ring (H^{11}) undergoes a significant downfield shift (δ = 8.67 and 7.84 ppm in **1a** and **2a**, respectively) relative to the corresponding free ligand (δ = 7.65 and 6.78 ppm in Br-HPBT and Me_2N-HPBT, respectively) in DMSO complexes **1a** and **2a**. This H^{11} resonance exhibits the expected platinum satellites with coupling constants ($^3J_{Pt\text{-}H}$) in the range J = 46–68 Hz, which is typical of orthometalated phenyl rings, in all the com-

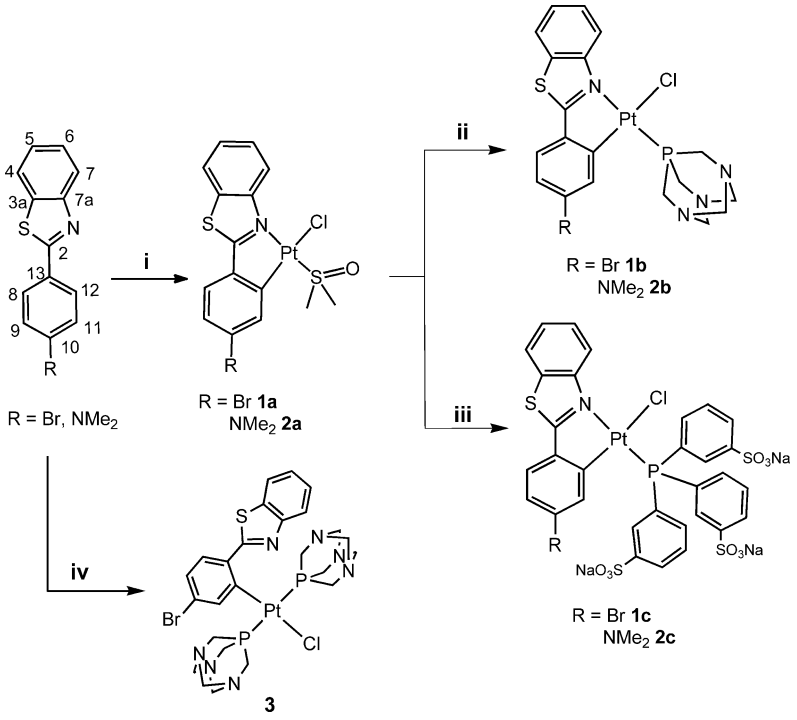

Scheme 1. Synthesis of **1**–**3**. Reagents and conditions: i) [{Pt(μ-Cl)(η^3-2Me-C_3H_4)}$_2$], toluene, reflux; then DMSO; ii) PTA, CH_2Cl_2, 20 °C; iii) P(*m*-$C_6H_4SO_3^-Na^+$)$_3$, acetone/H_2O, 20 °C; iv) [{Pt(μ-Cl)(η^3-2Me-C_3H_4)}$_2$], toluene, reflux; then PTA (see the Supporting Information for the experimental details).

plexes.[17] In **1a** and **2a**, the presence of a singlet for the proton at $\delta = 3.71$ and 3.68 ppm in **1a** and **2a**, respectively, with platinum satellites ($^3J_{Pt\text{-}H} \approx 25$ Hz) and one signal in the $^{13}C\{^1H\}$ NMR spectra at $\delta = 46.1$ and 46.2 ppm in **1a** and **2a**, respectively, ($^2J_{Pt\text{-}C} = 63$ and 64 Hz for **1a** and **2a**, respectively) provides evidence of the coordination of DMSO to platinum.[17,26] The expected proton resonances for the PTA ligand appear as a broad singlet (NCH_2N) and an AB system (PCH_2N, $J_{H\text{-}H} = 12$ Hz) in complex **2b**, whereas these resonances are isochronous in **1b** ($\delta = 4.63$ ppm). The $^{31}P\{^1H\}$ NMR spectra of **1b,c** and **2b,c** display a single resonance with a high $^1J_{Pt\text{-}P}$ splitting ($J = 4030$–4810 Hz), which is typical of a phosphorus atom in a *trans* position with respect to the nitrogen atom.[27] For complex **3**, the H^8 and H^{11} protons ($\delta = 8.25$ and 7.85 ppm, respectively) are slightly shifted downfield relative to the free ligand ($\delta = 7.97$ and 7.64 ppm, respectively) and display platinum satellites ($^4J_{Pt\text{-}H} = 17$ and $^3J_{Pt\text{-}H} = 73$ Hz for H^8 and H^{11}, respectively) in accordance with the C-coordination of the phenyl moiety to the Pt^{II} center. The mutually *trans*-PTA ligands are seen in the ^1H NMR spectrum as two resonances (a multiplet and singlet at $\delta = 4.31$ and 3.91 ppm for the NCH_2N and PCH_2N protons, respectively) and in the $^{13}C\{^1H\}$ NMR spectrum as a singlet ($\delta = 73.1$ ppm; *N*-CH_2N) and the expected virtual triplet ($\delta = 49.2$ ppm, $^{1+3}J_{C\text{-}P} = 20$ Hz; P–CH_2). The ^{31}P NMR resonance at $\delta = -64.9$ ppm displays a smaller $^1J_{Pt\text{-}P}$ coupling constant ($J = 2705$ Hz) relative to **2**, in accordance with the lower *trans* influence of the phosphorus atom.

The structures of complexes **1a,b**, **2a,b**, and **3** were established by X-ray diffraction studies (Figure 1). Table S1 (see the Supporting Information) lists a selection of relevant bond lengths and angles, and Table S2 some crystallographic data and refinement parameters. In the case of PTA derivatives **1b** and **2b**, two independent molecules were found in the asymmetric unit with distances and angles comparable within experimental error. For simplicity, only one of the two molecules (denoted as **A**) is given in Figure 1. The data and figures for molecules **B** of **1b** and **2b** are given in the Supporting Information. In complexes **1** and **2**, the platinum center shows a distorted square-planar environment formed by the cyclometalated ligand (Br-PBT or Me_2N-PBT), a chloride atom, and the sulfur atom of the DMSO ligand in **1a** and **2a** or the phosphorus atom of the PTA molecule in **1b** and **2b** in a *cis* position to the metalated carbon atom. The phenylbenzothiazole ligand displays a more planar disposition in complexes **1a,b** than in **2a,b**. Thus, the deviations of the benzothiazole (BT) group with respect to the platinum coordination plane are 9.64 and 5.12° in **1a** and **1b**, respectively, and the angles between the Ph ring and the BT group are 1.96 and 5.61° in **1a** and **1b**, respectively, whereas these angles are 25.91 and 17.64° and 22.41 and 4.91° in complexes **2a** and **2b**, respectively. Bond lengths of the donor atoms to the platinum center (Pt-Cl: 2.3923(14)–2.400(3); Pt-S: 2.2119(13)–2.2133(12); Pt-P: 2.2091(14), 2.207(3); Pt-C: 2.016(4)–2.036(12) Å) are within the normal ranges expected for cyclometalated complexes.[3d,17,22b,24,28]

The S2–O1 bond length is shortened in **1a** and **2a** relative to free DMSO,[29] and the amino nitrogen atom in the dimethylamine substituent is trigonal planar in **2a** and **2b**, with a short C–N bond length (1.363(6) and 1.384(15) Å in **2a** and **2b**, respectively) and a small torsional angle of 11.7 (C10-C11-N2-C14

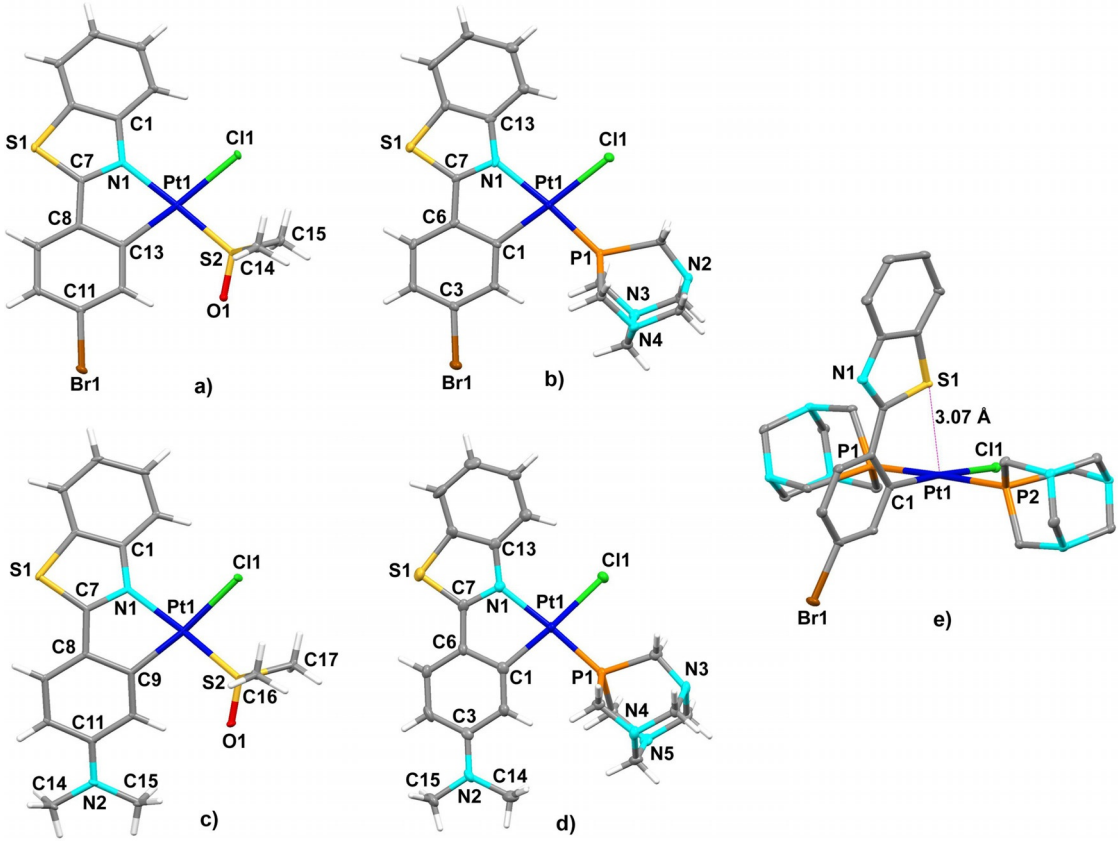

Figure 1. Molecular structures of: a) **1a**, b) **1b**·0.5 $CHCl_3$ (molecule **A**), c) **2a**, d) **2b**·$CHCl_3$ (molecule **A**), and e) **3**·$CHCl_3$.

in **2a**) or 7.1° (C2-C3-N2-C14 in **2b**). Complexes **1a**,**b** and **2b** show a certain degree of π stacking between the cyclometalated ligands of adjacent molecules in the crystal structure, whereas no stacking is observed for **2a** (see Figures S2–S6 in the Supporting Information). The molecules in the crystal structure of **1a** form dimers related by symmetry (intermolecular separation = 3.4–3.5 Å) with moderate Pt···Pt separation (3.703 Å), which are packed in columns with longer Pt···Pt distances (7.7 Å). Molecules **A** and **B** in **1b** of adjacent asymmetric units are stacked (3.3–3.5 Å) in columns (**A**···**A**···**B**···**B**) in a head-to-head manner. The extended packing in **2b** is observed between the two types of molecule (**A**···**A**) and (**B**···**B**).

The molecular structure of *trans*-[Pt(Br-PBT)Cl(PTA)$_2$]·$CHCl_3$ (**3**·$CHCl_3$; see Figure 1e and Table S1 in the Supporting Information) exhibits a slightly distorted square-planar geometry with a *trans* arrangement of two PTA ligands, a chloride atom, and a nonchelated 2-(4-bromophenyl)benzothiazole ligand coordinated through the C1 atom of the phenyl ring. Upon nitrogen decoordination, the pendant benzothiazole fragment is still coplanar with the phenyl group, but is rotated relative to the chelated complexes **1a**,**b** and **2a**,**b**, with the sulfur atom oriented toward the platinum center. The Pt···S distance (3.073 Å) is shorter than the Van der Waals limit (3.55 Å) and comparable to the distance reported for the penta-coordinated cation [Pt(ppy)(9S3)]$^+$ (9S3 = 1,4,7-trithiacyclononane)[30] (2.9518(17) Å). The Br-PBT group is essentially perpendicular to the platinum coordination plane (angle = 85.28°). The Pt–P bond lengths (2.2858(8) and 2.2807(8) Å) are marginally longer than those distances observed in **1b** and **2b** and are in the same range as those lengths found for related *trans*-Pt(PTA)$_2$ derivatives.[31] The steric bulk of the PTA ligands makes the presence of π···π intermolecular interactions difficult (see Figure S7 in the Supporting Information).

Photophysical properties

Absorption spectra

A summary of the UV/Vis absorption data of complexes **1**–**3** is given in Table S3 (see the Supporting Information), and the spectra of **1** and **2** are compiled in Figure 2 for comparison. All the complexes show high-energy intense absorptions ($\lambda <$ 360 nm, $\varepsilon \approx 10^4\ M^{-1}\ cm^{-1}$), attributed to ligand-based ^{1}IL (π–π*) transitions, as the free ligands show similar bands (Br-HBPT: $\lambda = 315$, 331 nm; Me_2N-HPBT: $\lambda = 357$ nm). The cyclometalated complexes **1** and **2** present a characteristic low-energy feature, notably red-shifted from the free-ligand absorption because of the cyclometalation and consequent perturbation from the metal center. The lowest-lying bands have higher molar absorptivities and are notably red-shifted in the Me_2N-PBT derivatives ($\lambda = 433$, 444 (**2a**), 427 (**2b**), 441 nm (MeOH, **2c**); $\varepsilon \approx 3 \times 10^4\ M^{-1}\ cm^{-1}$) relative to the Br-PBT complexes ($\lambda = 382$, 406 (**1a**), 392, 410 (**1b**), 385, 403_{sh} nm (MeOH, **1c**); $\varepsilon \approx 10^3\ M^{-1}\ cm^{-1}$), thus indicating a greater intraligand charge-transfer contribution due to a better interaction of the good electron-donating NMe_2 group with the aromatic moiety relative to that of the bromine atom. The charge-transfer nature of

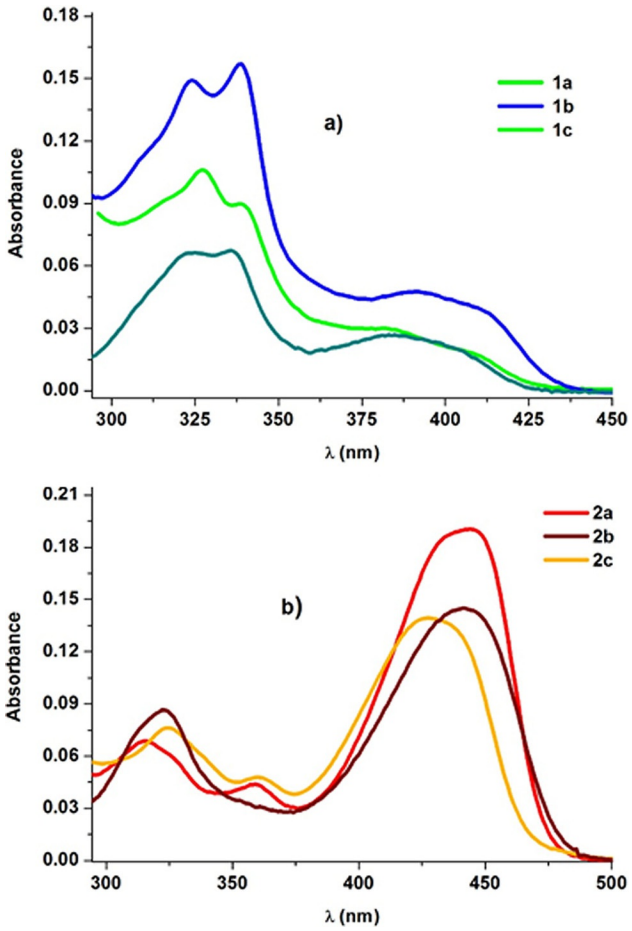

Figure 2. UV/Vis spectra of **1a,b** and **2a,b** in CH_2Cl_2 and **1c** and **2c** in MeOH (5×10^{-6} M) at 298 K.

the excitation was also supported by the slight negative solvatochromism in the absorption maxima of **2a** and **2c** with a blueshift as the polarity of the solvent increases (**2a**: $\lambda=446$ vs. 435 nm in toluene and MeOH, respectively; **2c**: $\lambda=441$ and 434 nm in MeOH and H_2O, respectively), thus suggesting a greater ground-state dipole moment relative to the excited state.[18a,32] According to previous studies[17,18b,32c,33] and time-dependent (TD)-DFT calculations on **1a** and **2a** (see below), the low-energy absorption in complexes **1a–c** is assigned to a ligand-centered (^{1}LC) transition mixed with a metal-to-ligand charge transfer (^{1}MLCT) [Pt→PBT] contribution, whereas this band has primarily ligand-based ^{1}ILCT charge-transfer character from the dimethylaminophenyl donating ring to the acceptor benzothiazole unit [Me_2N→PBT] for the (dimethylaminophenyl)benzothiazole derivatives **2a–c**. Complex **3** displays an extremely weak absorption feature ($\lambda=391$–410 nm; $\varepsilon\approx1\times10^3$ M^{-1} cm^{-1}), which is tentatively ascribed to a transition involving a platinum-to-ligand ^{1}MLCT (Pt→HC^N) charge transfer.

The influence of the concentration was examined with complex **2a**. Upon increasing the concentration of **2a** in CH_2Cl_2, a similar plot of the apparent absorbance at $\lambda=465$, 315, or 246 nm is observed, thus showing a relatively good agreement with Beer's law in the concentration range 5×10^{-6}–10^{-4} M (see Figure S8 in the Supporting Information). The fact that increasing concentration is not accompanied by a significant drop in the high-energy absorption region at approximately $\lambda=$ 250 nm indicates that although complex **2a** could undergo self-assembly through π····π stacking interactions with increasing concentration[34] (as suggested by the emission behavior), this behavior is not manifested in the ground-state UV/Vis spectra. As shown in Figure S8 (see the Supporting Information), similar effects were also noticed in the ^{1}H NMR spectra measured in CD_2Cl_2 by increasing the concentration from 5×10^{-4} to 5×10^{-2} M. An increase in the complex concentration results in a very slight upfield shift of approximately $\Delta\delta=$ 0.01 ppm of the signals that correspond to the phenyl ring and NMe_2 substituent, thus suggesting only a minor alteration (if any) of the observed chemical shifts on the NMR timescale.

Emission spectra

Emission data of complexes **1–2** in different media are summarized in Table 1 and Table S4 (see the Supporting Information), and representative spectra are presented in Figures 3–6 and Figures S9–S15 (see the Supporting Information). The Br-PBT derivatives **1a–c** exhibit a similar structured emission band in solution (**1a,b**: CH_2Cl_2; **1c**: MeOH (5×10^{-4} M)), glass, solid, and PMMA matrix, with maxima in the range $\lambda=532$–542 and

Table 1. Photophysical data of complexes **1** and **2** in degassed CH_2Cl_2 and PMMA (10 wt%).

Complex	Medium	T [K]	λ_{em} [nm] (ϕ, τ)
1a	CH_2Cl_2	298	430[a]
			532 (1.5%, 0.17 μs)
		77	544 (21.9 μs)
	PMMA	298	538 (14.6%, 14.9 μs)
1b	CH_2Cl_2	298	400 (4.1 ns)
			538 (1.9%, 0.03 μs)
		77	545 (20.3 μs)
	PMMA	298	536 (8.5%, 13.9 μs)
1c	MeOH	298	444 (<2 ns)
			532 (1.7%, 0.32 μs)
		77	526 (31.1 μs)
	PMMA	298	538 (11.4%, 13.5 μs)
2a	CH_2Cl_2[b]	298	474 (3.9%, <2 ns)
			574 (6.2%, 17.6 μs)
		77	470[a]
			562 (116.5 μs[c])
	PMMA	298	574 (53.3 μs)
2b	CH_2Cl_2[b]	298	472 (3.5%, <2 ns)
			565 (26.6 μs)
		77	464[a]
			558 (116.8 μs[c])
	PMMA	298	568 (41.1 μs)
2c	MeOH[b]	298	488 (2.2%, <2 ns)
			574 (15.8 μs)
		77	468[a]
			567 (140.8 μs[c])
	PMMA	298	572[a] (56.1 μs)
3	PMMA	298	536 (9.7%, 15.8 μs)

[a] Very weak emission. [b] Concentration: 5×10^{-6} M, emission dependent on the concentration (see text). [c] Averaged emission lifetime for the two-exponential decay determined by the equation $y=A_1$*exp$(-x/\tau_1)+A_2$*exp$(-x/\tau_2)+y_0$.

526–568 nm (at $\lambda = 298$ and 77 K, respectively) and vibronic progressions (1270–1360 cm^{-1}), which are indicative of a prevalent contribution from the cyclometalated ligand into the frontier orbitals associated with the emissive state. As an illustration, the room-temperature emission spectra for **1a–c** in doped PMMA films (10 wt%) and glass are shown in Figure 3 and Figure S9 (see the Supporting Information), respectively. The lifetimes recorded in PMMA at 298 K ($\tau = 14.9$, 13.9, and 13.5 μs for **1a–c**, respectively) are larger than in the solid state

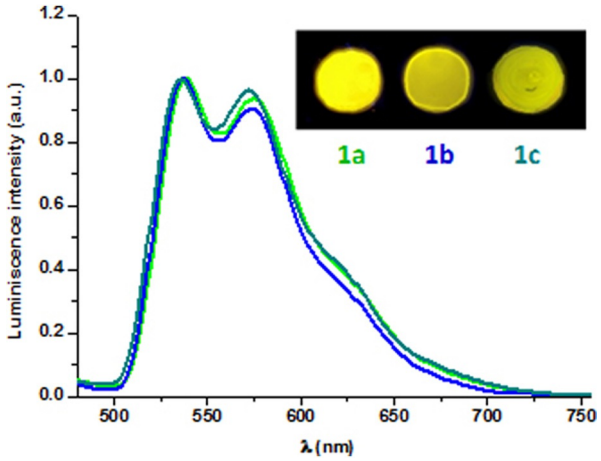

Figure 3. Normalized emission spectra of **1a–c** in poly(methyl methacrylate) (PMMA; 10% w/w) at 298 K ($\lambda_{ex} = 400$ nm).

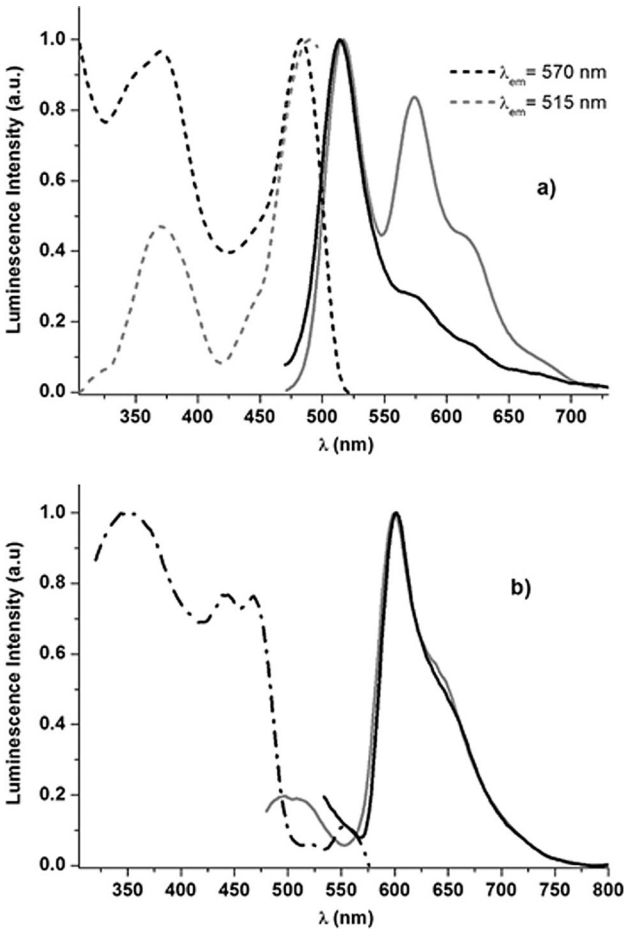

Figure 4. Normalized excitation (····) and emission (——) spectra of **2a** in the solid state (pristine sample, gray) and microcrystalline ground solid (black) at: a) 298, and b) 77 K.

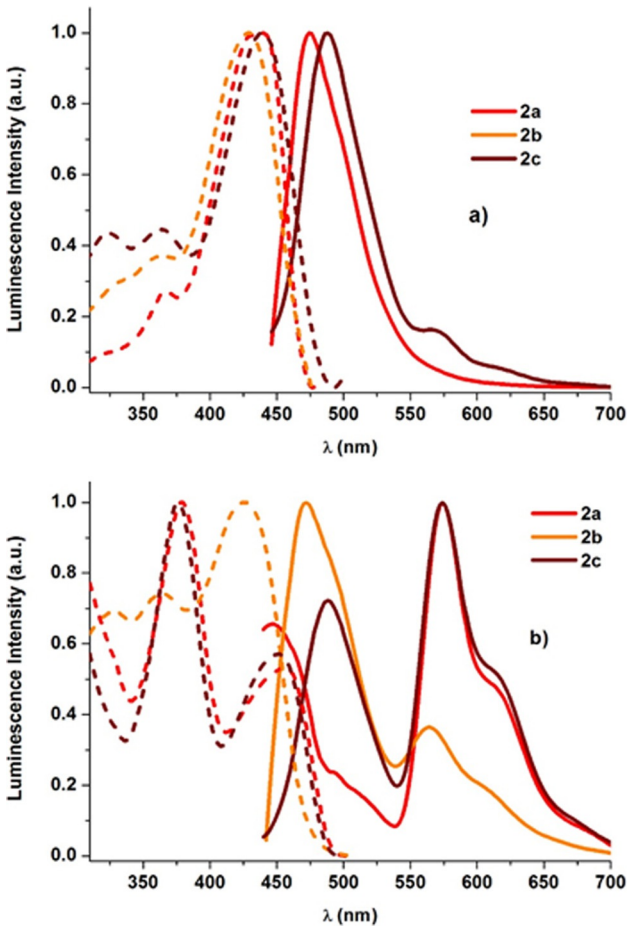

Figure 5. Normalized excitation (····) and emission (——) spectra of diluted solutions (5×10^{-6} M) of **2a**,**b** (CH_2Cl_2) and **2c** (MeOH) in: a) aerated, and b) deoxygenated solutions at 298 K ($\lambda_{exc} = 420$ nm and $\lambda_{em} = 570$ nm).

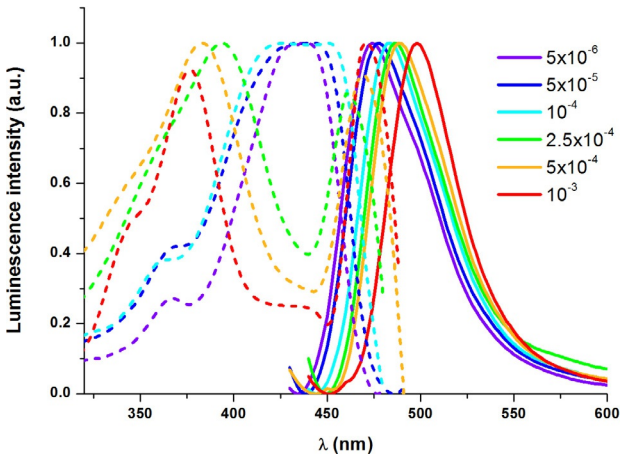

Figure 6. Normalized excitation (····) and emission (——) spectra of **2a** in CH_2Cl_2 at different concentrations at 298 K ($\lambda_{exc} = 420$ nm).

at 298 K ($\tau = 6.9$ and 7.6 μs (average values) for **1a**,**b**, respectively) and in fluid media ($\tau = 0.17$, 0.03, and 0.32 μs for **1a**–**c**, respectively), thus suggesting easier access to deactivation of the excited states in CH_2Cl_2 at 298 K. TD-DFT and DFT calculations on **1a** (see below), together with previous spectroscopic studies on similar complexes, support a predominant ^{3}LC nature with minor ^{3}MLCT character for the emission. We note that the emission spectra in solution show, in addition to the expected structured band in the yellow region ($\lambda = 532$, 538 (CH_2Cl_2), and 532 nm (MeOH) for **1a**–**c**, respectively), a small band in the blue region ($\lambda = 430$, 400, and 444 nm for **1a**–**c**, respectively) with a short lifetime ($\tau = 4.1$ and < 2 ns for **1b**,**c**, respectively) due to residual fluorescence (see Figure S10 in the Supporting Information).[35]

The Me_2N-PBT derivatives **2** emit in all media, except in a microcrystalline state at 298 K (see Table 1 and Table S4 in the Supporting Information). In rigid media (PMMA or solid 77 K), these systems exhibit vibronically structured profiles that are bathochromically shifted relative to the Br-PBT derivatives (i.e., $\lambda =$ 574, 568, and 572 nm for **2a**–**c** in PMMA respectively (Figure S11 in the Supporting Information), vs. $\lambda = 538$, 536, and 538 nm for **1a**–**c**, respectively), which are ascribed to an intraligand ^{3}ILCT excited state localized on the benzothiazole group [Me_2N-PBT→PBT], based on DFT/TD-DFT calculations (see below). The redshift can be attributed to the incorporation of the electron-donating NMe_2 group, which destabilizes the HOMO energy through electron donation. This assignment is also supported by the long radiation decay times ($\tau = 53.3$, 41.1, and 56.1 μs for **2a**–**c**, respectively), clearly longer than for complexes **1**.

Only **2a**, as a powder, is emissive in the solid state at 298 K. The pristine solid **2a** exhibits a dual emission formed by a band centered at $\lambda = 515$ nm, with a short lifetime of approximately 7 ns, which suggests fluorescence and a long-lived lower-energy band ($\lambda = 575$ nm, $\tau = 12.2$ μs) due to phosphorescence (Figure 4a). In support of this assignment, the excitation-spectra monitoring of both bands are coincident. Upon cooling at 77 K, the fluorescence band decreases and the phosphorescence located at $\lambda = 600$ nm mainly contributes to the intense emission observed. The emission is close to the emission observed for **2b**,**c** in the solid state at 77 K ($\lambda = 590$ and 596 nm for **2b**,**c**, respectively). Interestingly, microcrystalline solid **2a** is, as **2b**,**c**, nonemissive at 298 K. However, upon grinding this microcrystalline solid, the emission is triggered, to which the fluorescence band mainly contributes (Figure 4a). At low temperature (77 K), the phosphorescence band is again predominant (Figure 4b).

In aerated diluted solutions (**2a**,**b**: CH_2Cl_2; **2c**: MeOH (5×10^{-6} M)) at 298 K, complexes **2a**–**c** display only a structureless emission in the blue region ($\lambda = 474$, 472, and 488 nm for **2a**–**c**, respectively; Figure 5a). Due to the small Stokes shift ($\lambda = 30$, 45, and 49 nm for **2a**–**c**, respectively) and short lifetime in the nanosecond region, the emission is attributed to intraligand ^{1}ILCT fluorescence. However, these complexes also exhibit a weak low-energy phosphorescent emission in degassed solutions, which we attributed to a mixed ^{3}ILCT/^{3}MLCT emissive state (Figure 5b). In support of this assignation, the excitation spectra monitoring at these low-energy bands differ from those observed monitoring the ^{1}ILCT fluorescence. The weak or lack of phosphorescence in solution for complexes **2a**–**c** is not unexpected and can be rationalized by easy access to several quenching mechanisms. First, the lone pair of electrons on the NMe_2 group is delocalized (see the X-ray diffraction image) within the phenyl ring at the HOMO orbital in the ground state S_0. It is well-known that the S_1 state (^{1}ILCT) might evolve with a torsional motion of the amino group upon excitation, thus leading to population of a dark twisted intramolecular state, in which the lone pair of electrons on the nitrogen atom is no longer delocalized within the phenyl ring, thus enhancing the radiationless deactivation to the ground state.[36] Second, the square-planar geometry of the Pt^{II} center with a d^8 electronic configuration allows easy access to collisional interactions with solvent molecules and is enhanced in these complexes by the electron-donating nature of the amine group, thus favoring efficient deactivation.[37] Finally, another route to decrease the phosphorescence in aerated solutions results from the relative ease by which the triplet excited state undergoes triplet–triplet quenching by the oxygen moiety, which is facilitated by the long phosphorescence lifetimes ($\tau = 15.8$–26.6 μs).[38]

The effect of the concentration on emissive behavior has been examined for complexes **2a**,**b** under aerobic conditions. For **2a**, the effect of the concentration on the emission in CH_2Cl_2 is more significant than for the absorption (Figure 6). Upon increasing the concentration from 5×10^{-6} to 10^{-3} M, the fluorescence emission maxima red-shifted from $\lambda = 474$ to 498 nm. Interestingly, the excitation spectrum changes remarkably at concentrations above 10^{-4} M, exhibiting two pronounced maxima at approximately $\lambda = 380$–390 and 475 nm, respectively. A similar behavior was observed for **2b** (see Figure S12 in the Supporting Information). In reference to previous studies with cycloplatinated(II) complexes,[34,39] this behavior suggests that the fluorescence observed at high concentration for complex **2a** (and also **2b**) in solution is generated by an aggregate, likely driven by π····π and/ or Pt···Pt interactions in the ground state. As expected, the formation of aggregates also has a profound effect on the emission in the glass state at 77 K; however, this effect is more noticeable for **2a** than for **2b**, likely due to the presence of the bulkier PTA ligand in **2b** (see Figures S12b and S13 in the Supporting Information). In dilute solution (5×10^{-6} M, 77 K), **2a** displays weak fluorescence and an intraligand ^{3}ILCT phosphorescence due to the monomer ($\lambda_{max} = 562$ nm). Upon increasing the concentration, the fluorescence disappears and the emission due to the monomer decreases in intensity with a slight redshift in its maximum ($\Delta \approx 15$ nm), whereas new low-energy features develop ($\lambda \approx 620$ nm at 10^{-4} M; $\lambda \approx 650$ nm at 10^{-3} M, see Figure S13a in the Supporting Information), which could be attributed to metal/metal-to-ligand charge transfer transitions (^{3}MMLCT), associated with the formation of π····π stacking and platinum–platinum contacts in the newly formed species. Although excimer formation cannot be ruled out, in support of ground-state aggregation, the excitation spectra profiles monitoring at these new bands differ (see Figure S13b in the Supporting In-

formation) and are found at lower energies relative to the observed for the monomer in dilute solution monitoring at $\lambda =$ 560 nm;[35,40] furthermore, the average decays lifetime are larger.

The effect of the solvent on the spectral characteristics of aerated 5×10^{-6} M solutions of **2a** was also examined. In agreement with the charge-transfer nature (CT), the maximum emission of the fluorescence band at 298 K (from $\lambda = 472$ nm in toluene to 484 nm in MeCN) and the ^{3}ILCT phosphorescence in the glass state at 77 K ($\lambda = 555$ and 564 nm in toluene and MeCN, respectively) follow a similar tendency, exhibiting a slight bathochromically shift with increasing solvent polarity (see Figure S14 in the Supporting Information), thus pointing to a stronger stabilization of the excited state in polar solvents.

Complex **3** is only weakly emissive in the solid state, CH_2Cl_2, glass, and a PMMA film (10% w/w; details are given in Table 1 and Table S4 and Figure S15 in the Supporting Information) and is assigned to a metal-perturbed ^{3}LC excited state.

Effect of acid/base concentration

The optical properties of the Me_2N-PBT complexes **2** should change upon protonation, and we decided to examine the behavior of the less-complicated complex **2a** toward *para*-toluensulfonic acid (PTSA) in acetonitrile solution with under aerobic conditions and toward hydrogen chloride gas ($HCl_{(gas)}$) in the solid state. Upon the addition of PTSA (above 2 equiv.) to a solution of **2a** in CH_3CN, the low-energy ^{1}ILCT absorption band at $\lambda = 440$ nm decreases in intensity, whereas new bands at high energy develop ($\lambda \approx 330$ nm) with a well-defined isosbestic point at $\lambda = 342$ nm, which is indicative of a clean conversion of **2a** into its protonated form (Figure 7). The protonation of the amino group decreases its electron-donating ability, and the CT character of the transition, which, according to calculations, has a mixed ^{1}LC/^{1}MLCT nature with some ^{1}L′LCT [Cl→NHMe$_2$-PBT] contribution in the protonated ion **2a-H$^+$**. The process is reversible and the initial spectrum was recovered upon the addition of triethylamine. The blue initial fluorescence of **2a** shows also notable proton-induced quenching as the amount of PTSA increases, with almost total elimination when 20 equivalents of PTSA are added. With a large excess of acid, a weak orange emission is observed (Figure 8). The

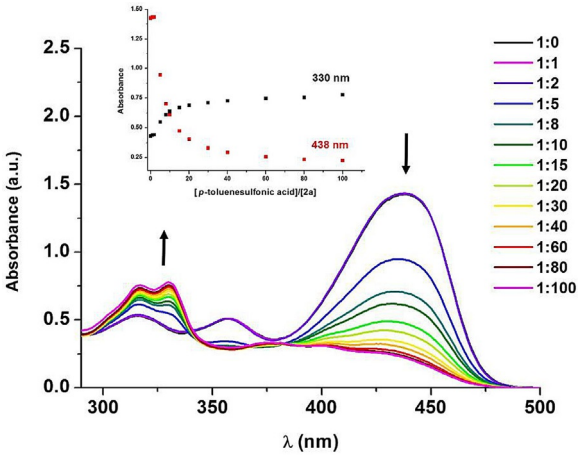

Figure 7. UV/Vis absorption changes of **2a** in acetonitrile (5×10^{-5} M) with increasing concentrations of PTSA. Inset: plots of absorbance at $\lambda = 438$ and 330 nm against the total concentration of PTSA.

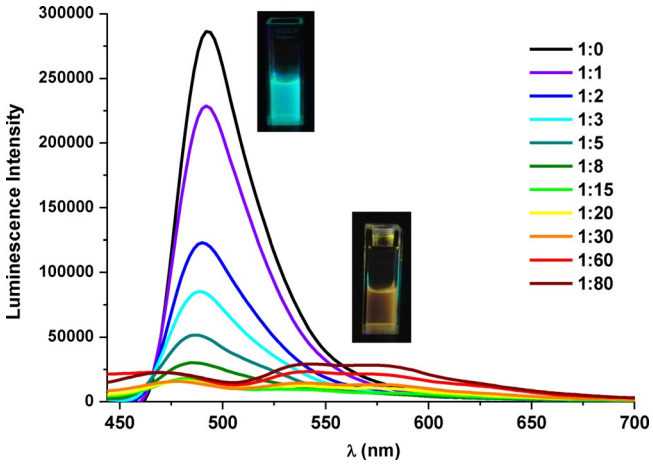

Figure 8. Emission spectra of **2a** in acetonitrile (5×10^{-4} M) with increasing PTSA concentration.

maxima ($\lambda = 542$ nm) and the lifetime ($\tau = 0.27$ μs) are close to that found for **1a**, and the transition was thus ascribed to a phosphorescent transition (^{3}LC/^{3}MLCT) in the generated cation **2a-H$^+$**.

As noted above, microcrystalline solid **2a** is not emissive, whereas amorphous solids (pristine or ground samples) are only weakly emissive (Figure 4) at room temperature. During preliminary studies of the interaction of solid **2a** with vapors of $HCl_{(gas)}$, we observed an initial enhancement of the emission. However, a nonemissive yellow solid was formed, which immediately became a dark garnet in air, upon prolonged exposure of **2a** to $HCl_{(gas)}$ (excess) in a closed system. Slow crystallization of this solid afforded red garnet crystals, which were identified by single-crystal X-ray diffraction studies as the unexpected Pt^{IV}/dimethyl sulfide complex *fac*-[Pt(Me$_2$N-PBT-κ*C*,*N*)Cl$_3$(SMe$_2$)] (***fac*-4**; the data were of insufficient quality, therefore only the connectivity of atoms is presented in Figure S16; see the Supporting Information), the formation of which implies a formal oxidation of Pt^{II} to Pt^{IV} and deoxygenation of DMSO to afford dimethyl sulfide.

Metal-mediated deoxygenation of sulfoxides is a known reaction with importance in organic synthesis[41] and is also biologically relevant to understanding the oxotransference mechanism in the active site of the molybdenum-dependent DMSO reductase.[42] In platinum chemistry, these reactions usually proceed under harsh conditions; however, it is worth mentioning that Ryabov and co-workers found that cyclometalated oxime complexes ([Pt(C$_6$H$_3$-2-CMe=NOH-5-R)Cl(Me$_2$S=O)]) undergo deoxygenation of DMSO in the presence of HCl in methanol under mild conditions (40–60 °C), thus yielding Pt^{IV}/dimethyl sulfide complexes *fac*-[Pt(C$_6$H$_3$-2-CMe=NOH-5-R)Cl$_3$(Me$_2$S)].[43] A multistep intermolecular process involving the insertion of the

S=O moiety of DMSO into a Pt^{IV}–H intermediate species was suggested as a likely mechanism pathway. Not unexpectedly, ***fac*-4** was also obtained in moderated yield by heating **2a** with an excess of HCl (1:10) in MeOH to reflux for 4 h (see the Experimental Section in the Supporting Information). The most significant feature in the ^{1}H NMR spectrum of ***fac*-4** relative to precursor **2a** is the remarkable shielding of the H^{11} signal due to the loss of the oxygen atoms in the mutual *cis* ligand (SMe_2 vs. Me_2S=O) with concomitant decrease in the $^3J_{Pt\text{-}H}$ coupling constant (J=30 vs. 53 Hz in ***fac*-4** and **2a**, respectively), which is consistent with the change from Pt^{II} to Pt^{IV}, and two signals at δ=2.30 and 2.25 ppm, with similar Pt-H couplings (J=37 and 36 Hz) from the diasterotopic methyl groups of the coordinated SMe_2 ligand. To obtain more information on the process that lead to **4**, we carried out the reaction of **2a** with $HCl_{(gas)}$ under controlled conditions and the results are summarized in Scheme 2 (see Figure S17 in the Supporting Information for the ^{1}H NMR spectra).

When a ground microcrystalline solid sample of **2a** was exposed to $HCl_{(gas)}$ (generated from a 32% aqueous solution) for 10 min at room temperature, a remarkable emission enhancement with a visual color change was observed (Scheme 2 i) due to the relatively fast formation of **2a-H$^+$Cl$^-$** upon protonation of the amine group (characteristic shifts for the H^{11} and H^9 protons close to the NMe_2 unit were found). Switching off the weak fluorescence of **2a** (ϕ=2.1%) takes place with triggering of a more intense structured band in the orange range (λ_{max}= 532, 570 nm; ϕ=11%) with a long-lived decay (0.58 μs (average value)) ascribed to ^{3}LC/^{3}MLCT emission of **2a-H$^+$Cl$^-$**. At 77 K, the emission of **2a-H$^+$Cl$^-$** is blue-shifted (λ=572 nm) relative to the ^{3}ILCT **2a** (λ=600 nm; see Figure S18 in the Supporting Information). Prolonged exposure of **2a** to $HCl_{(gas)}$ (≈12 h) produces a nonemissive pale-yellow solid, identified as the protonated Pt^{IV}/dimethyl sulfide complex *mer*-[Pt(Me_2H^+ *N*-PBT-κ*C*,*N*)$Cl_3(SMe_2)$] (***mer*-4-H$^+$ Cl$^-$**; Scheme 2 ii). The ^{1}H NMR spectrum of this complex reveals that the most distinctive signals are the amine proton (δ=3.72 ppm, br); a singlet for the equivalent two methyl groups of the coordinated SMe_2 group at δ=2.83 ppm with a $^3J_{Pt\text{-}H}$ coupling constant of 36 Hz, consistent with a *trans* disposition to the nitrogen atom of the cyclometalated ligand; and the signal with Pt satellites due to H^{11}, which is shielded (δ=7.8 ppm, $^3J_{Pt\text{-}H}$=37 Hz) relative to the DMSO precursors, likely due to the presence of a coordinated SMe_2 group. Upon treatment of (***mer*-4-H$^+$Cl$^-$**) with a stream

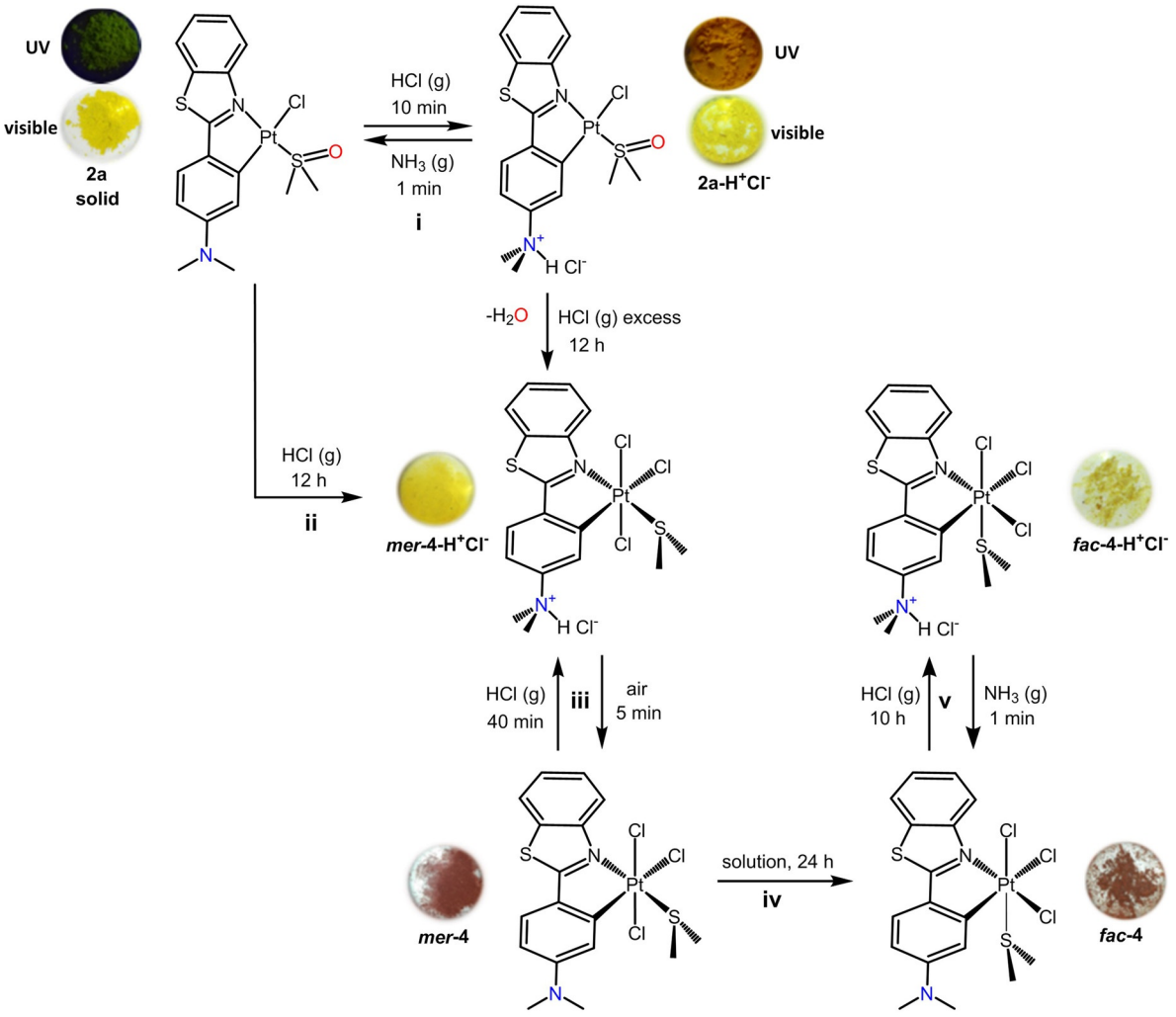

Scheme 2. Reactions of **2a** (ground microcrystalline solid) exposed to hydrogen chloride gas (generated from a 32% aqueous solution).

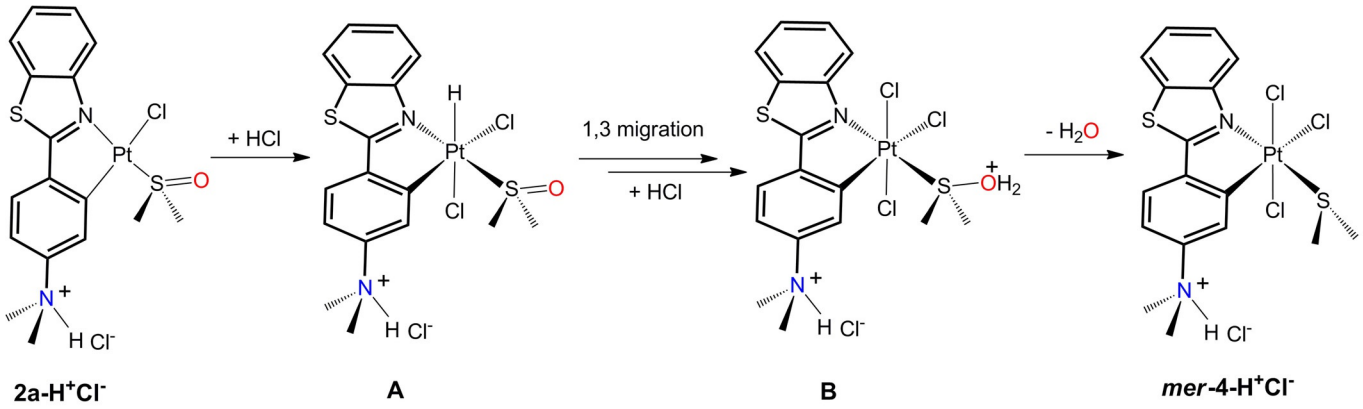

Scheme 3. Proposed mechanism for the reaction of **2a** with excess HCl.

of air for 5 min, relatively fast deprotonation and loss of HCl occurs, thus leading to a dark-red solid, identified as the geometric isomer ***mer*-4**. This transformation was reversible, although notably slower for the protonation step (Scheme 2 iii). Complex ***mer*-4** displays the H^{11} ($\delta = 7.14$ ppm, $^{3}J_{Pt\text{-}H} = 30$ Hz) and the NMe_2 protons ($\delta = 3.24$) shifted upfield relative to ***mer*-4-H$^+$Cl$^-$**, whereas the equivalent methyl groups of the SMe_2 functionality do not shift (see Figure S17 in the Supporting Information). Finally, we found that ***mer*-4** gradually isomerizes in solution to the thermodynamically more stable and sparingly soluble final complex ***fac*-4**. In the presence of HCl vapor for an extended period of time (10 h), the color of the solid changes from red-garnet to yellow, probably by protonation to ***fac*-4-H$^+$Cl$^-$** (Scheme 2 iv, v). Based on previous studies on the oxidation of a cyclometalated Pt^{II} moiety, we suggest that the formation of the Pt^{IV} species likely involves further protonation of the Pt^{II} center in the initial **2a-H$^+$Cl$^-$** with simultaneous coordination of the chloride group to afford the key Pt^{IV}/hydride intermediate (Scheme 3 **A**). Pt^{IV}/hydride complexes have been frequently invoked and characterized in many catalytic reactions.[44] The final deoxygenation process might be driven by subsequent 1,3 migration of the hydride group to the S=O double bond, thus yielding a (*S*)-hydroxydimethyl group, which easily protonates in presence of HCl (Scheme 3 **B**) and leaves H_2O and the dimethyl sulfide complex ***mer*-4-H$^+$Cl$^-$**.

The UV/Vis absorption spectra of complexes **4** (in CH_2Cl_2) feature a strong low-energy absorption band at $\lambda = 427$ or 421 nm (***fac*-4** and ***mer*-4**, respectively), ascribed with the support of theoretical calculations to a mixture of transitions mainly with ^{1}ILCT [Me_2N-PBT→PBT] character.

Computational calculations

To obtain a better understanding of the photophysical properties of the complexes, we carried out DFT and TD-DFT theoretical calculations at the B3LYP/(6-31G** + LANL2DZ) level in the presence of the solvent (CH_2Cl_2) on complexes **1a** and **2a**, the **2a**–**2a** dimer, the protonated form **2a-H$^+$**, and ***fac*-4** (see the Experimental Section in the Supporting Information for full computational details). The structures of **1a** and **2a** were optimized and reproduced the bond lengths and angles determined by X-ray diffraction, reasonably well (see Table S5 and Figure S19 in the Supporting Information). The optimized structures of **2a** are planar in the S_0, S_1, and T_1 states, which is in agreement with the crystal geometry, even starting from a model with the $N(CH_3)_2$ group twisted (perpendicular to the phenyl ring). However, protonation of the dimethylamino group lead to a rotation of the $N(CH_3)_2$ group around the C–N bond (angle between the Ph ring and $N(CH_3)_2$ group: 88 (S_0) and 89° (T_1) in **2a-H$^+$** vs. 6.37 (X-ray), 0 (S_0), and 2° (T_1) in **2a**), with pyramidalization of the nitrogen atom (51° (S_0, T_1) in **2a-H$^+$** vs. 11.18 (X-ray), 0 (S_0), and 2° (T_1) in **2a**).

Selected molecular orbitals (isosurface plots) are represented in Figure 9 and Figures S20–S24 (see the Supporting Information). The composition of the molecular orbitals from atomic-orbital contributions and the properties of selected excited states are collected in Tables S6 and S7 in the Supporting Information, respectively. The HOMO in **1a** is mainly located on the PBT ligand and the Pt center (68 and 21%, respectively), and the LUMO is mainly centered on the π-electron-accepting benzothiazole group of the PBT ligand (57 and 34% on the BT and Ph groups, respectively). The lowest-energy singlet transition calculated in CH_2Cl_2 (S_1: $\lambda = 392$ nm), close to the experimental value ($\lambda = 406$ nm; see Figure S25 in the Supporting Information), arises primarily from a HOMO to LUMO transition (92%); therefore, this transition is mainly attributed to a mixed ligand-centered ^{1}LC and metal-to-ligand ^{1}MLCT [Pt→PBT] transition. The HOMO in **2a** is delocalized over the Me_2N-PBT unit, with a notable contribution of the donor Me_2N substituent (22, 44, and 32% from the BT, Ph, and Me_2N groups, respectively), whereas the HOMO-1 is centered on the phenyl group, the chloride ligand, and the platinum center (42, 12, and 38%, respectively). The LUMO is mainly centered on the π-electron-accepting benzothiazole unit of the PBT ligand (57 and 29% on the BT and Ph groups, respectively). For this complex, the lowest-energy singlet transition ($\lambda = 411$ (calcd) vs. 433 nm (exp.)), to which the HOMO-to-LUMO excitation contributes, is assigned as an intraligand ^{1}ILCT transition [Me_2N-PBT→PBT], whereas the bands at approximately $\lambda = 347$ nm have ^{1}LC/^{1}MLCT character.

To understand the effect of self-assembly at high concentration, theoretical calculations on the **2a**–**2a** dimer were carried

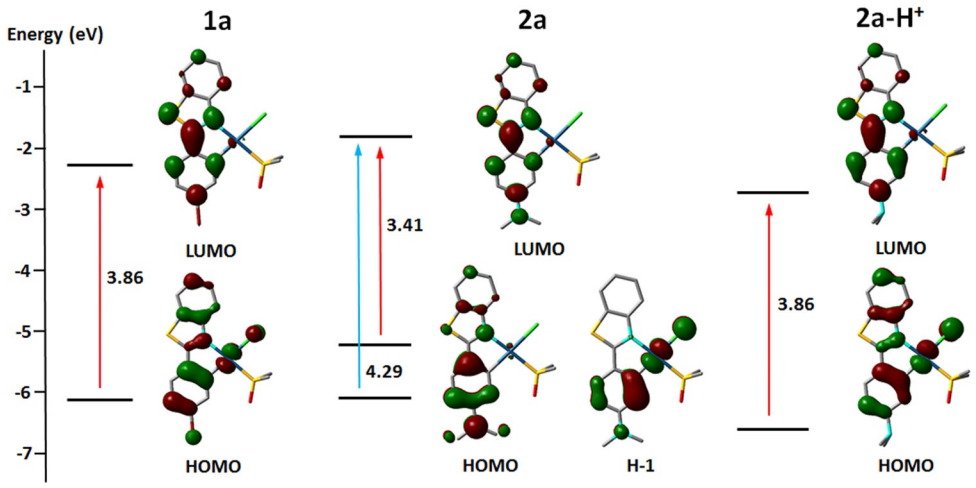

Figure 9. Schematic representation of selected frontier orbitals of **1a**, **2a**, and **2a-H$^+$**.

out. Both the HOMO and HOMO-1 are delocalized over the Me_2N-PBT fragment of each unit in the dimer (11, 22, and 16% on the BT, Ph, and Me_2N groups, respectively), whereas the LUMO and LUMO+1 are mainly centered on the π-electron-accepting benzothiazole group of each unit (LUMO: 28, 14, and 3% on the BT, Ph, and Me_2N groups, respectively). The lowest-energy singlet transition calculated in CH_2Cl_2 is slightly red-shifted relative to the monomer ($\lambda = 425$ vs. 411 nm), but presents a small oscillator strength. This transition and the inner intense transition at $\lambda = 402.5$ nm (S_4) have mixed contributions (HOMO, H-1→LUMO, LUMO+1), thus retaining the intraligand charge-transfer character ^{1}ILCT [Me_2N-PBT→PBT]. The small modification of the frontier orbitals in the dimer **2a**–**2a** relative to the monomer **2a** is in accord with the negligible influence of the concentration on the absorption profile observed experimentally.

Protonation of the NMe_2 group in **2a** (i.e., **2a-H$^+$**) modifies the nature of the HOMO, now located on the PBT unit (59%) with a remarkable contribution from the platinum center and the chloride ligand (28 and 11%, respectively), whereas the LUMO is similar to **2a** (see Table S6 in the Supporting Information). The HOMO is stabilized by 1.36 eV more than the LUMO (by 0.93 eV) relative to **2a**. Therefore, the low-energy feature is calculated to be blue-shifted relative to **2a** ($\lambda = 392$ vs. 411 nm; see also Figure S25 in the Supporting Information) and can be assigned as mixed ^{1}LC/^{1}MLCT with minor ^{1}L'LCT [Cl→PBT] contribution.

Due to the oxidation of the Pt^{II} center to Pt^{IV} in complex ***fac*-4**, the LUMO (and also LUMO-1) is mainly located on the platinum center with moderate contribution from the sulfur (SMe_2) and chloride atoms, whereas the Me_2N-PBT ligand contributes to the HOMO and HOMO-1. The HOMO→LUMO transition (S_1) is calculated at very low energy ($\lambda = 807$ nm) with minimal oscillator strength. For this complex, the most intense calculated excitations are S_{10} and S_{11} ($\lambda = 398$ and 393 nm, respectively), which can be associated with the very intense low-energy experimental band at $\lambda = 427$ nm ($\varepsilon = 34.5 \times 10^3$ M^{-1} cm^{-1}). These excitations are of mixed configuration (HOMO→LUMO+2, H-8, H-4→LUMO) and allow this band to be ascribed mainly to a mixture of intraligand (Me_2N-PBT→PBT) and halide-to-ligand (SMe_2)–metal [Cl→SMe_2,Pt] (^{1}ILCT/^{1}X(L'+M)CT) with some ligand (Me_2N-PBT)-to-metal (^{1}LMCT) contribution.

The calculated electronic energies of the optimized lowest T_1 state relative to the S_0 optimized state are close to the experimental values ($\lambda = 539$, 581, and 542 nm (calcd) vs. $\lambda = 538$, 574, and 532 nm (exp.) for **1a**, **2a**, and **2a-H$^+$**, respectively). The spin-density distribution is essentially centered on the cyclometalating ligand with small (**1a**, **2a-H$^+$**) or negligible (**2a**) contribution of the platinum center (0.1130, 0.0485, and 0.1269 eV for **1a**, **2a**, and **2a-H$^+$**, respectively; Figure 10). The composition of the SOMO and SOMO-1 (see Table S8 and Figure S26 in the Supporting Information) identifies the excitation as HOMO→LUMO for **2a**, which allows the phosphorescence of **2a** ($\lambda = 574$ nm) to be determined as ^{3}ILCT character. To explain the fluorescence observed in CH_2Cl_2 at 298 K ($\lambda = 474$ nm), TD-DFT excited-state optimizations were performed for the lowest-energy singlet state (S_1). The calculated $S_1 \rightarrow S_0$ emission energies ($\lambda = 525$ nm) indicate qualitative agreement with the experimental maxima ($\lambda = 474$ nm). The composition of the SOMO and SOMO-1 (see Table S8 and Figure S26 in the Supporting Information) identifies the excitation as HOMO→LUMO+1 for **2a** (S_1), which allows the fluorescence of **2a** to be determined as ^{1}ILCT with some ^{1}LMCT character. For **1a** and **2a-H$^+$**, the small contribution of the platinum center (and also

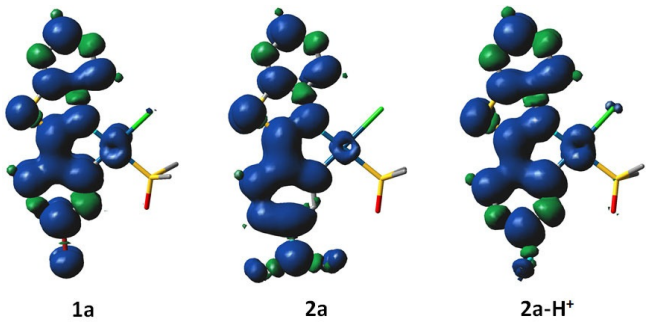

Figure 10. Spin-density distribution for the lowest triplet excited state in **1a**, **2a**, and **2a-H$^+$**.

the Cl ligand in **2a-H$^+$**; SOMO-1: 8% Pt in **1a**; 10% Pt, 1% Cl in **2a-H$^+$**) in the optimized T_1 state contrasts with the higher contribution from the platinum center in the optimized S_0 geometry (HOMO; Pt: 21 (T_1) and 28% (S_0) in **2a-H$^+$**), thus suggesting a higher distortion upon excitation. Thus, the emission for **1a** and **2a-H$^+$** has ^{3}LC character with minor ^{3}MLCT contribution.

Biological properties

Cytotoxicity tests (MTS assay)

In view of previous results that described promising anticancer activities for a variety of cyclometalated platinum(II) complexes,[2a,k,l,3,5–7,17] we checked the antitumoral properties of compounds **1a**–**c** and **2c** toward human-lung cell lines adenocarcinomic alveolar basal epithelial cells (A549) and epitheloid cervix carcinoma cells (HeLa) in vitro by using the [3-(4,5-dimethylthiazol-2-yl)-5-(3-carboxymethoxyphenyl)-2-(4-sulfophenyl)-2*H*-tetrazolium] hydrolysis method (MTS assay), with cisplatin as a reference. The IC_{50} values were determined after cellular exposure to the compounds for 72 h (see Table 2 and Figure S27 in the Supporting Information). The cisplatin IC_{50} dose toward A549 cells (6.45 μM) was previously reported by us[17] and was similar for the HeLa cells to values reported by others.[45] Although complexes **1a**,**c** and **2c** were nontoxic, **1b** and **2a**,**b** displayed some anticancer activity, thus showing IC_{50} values higher than cisplatin and with similar values in both cell lines. Compounds **1b** and **2a**,**b** showed steeper curves of cytotoxicity relative to cisplatin, an effect observed in both cell lines (see Figure S27 in the Supporting Information). These results indicate a highly homogeneous response toward these compounds and may suggest a different cytotoxic mechanism of action relative to cisplatin. Shallow concentration–response relationships were previously interpreted as a sign of multiple cellular targets[46] and therefore could explain the lower cytotoxic activity relative to cisplatin, a chemotherapeutic drug known to have several molecular mechanisms of action.[47] No correlation between water solubility and cytotoxicity can be inferred. In fact, the PTA-containing complexes **1b** (IC_{50} = 53.93 and 55.39 μM in A549 and HeLa cells, respectively) and **2b** (IC_{50} = 71.83 and 61.53 μM in A549 and HeLa cells, respectively) were the most cytotoxic compounds despite of their much lower solubility in water.

Fluorescence-microscopy cellular localization

The intracellular localization of **1** and **2** was also assessed by fluorescence microscopy. To this aim, the compounds were incubated at concentrations of 100 μM with the DNA binder Hoechst 33258 (3.2 μM) in A549 and HeLa cells for 1 h. Living-cell preparations were examined with a fluorescence microscope,[17] suitable for alternate imaging with Nomarski DIC transmitted light, and with green, red (data not shown), and blue fluorescent emitted light. The superimposition of images obtained with Nomarski visualization and Hoechst staining of nuclear DNA helped to ascertain the site of fluorescence at subcellular levels. The results of cellular localization of complexes **1a**–**c** and **2a**–**c** are shown in Figure 11 and summarized in Table 2. None of the complexes showed blue-light emission in the spectral region in which Hoechst 33258 bound to DNA is visible (λ_{em} = 461 nm);[48] conversely, the Hoechst stain did not show emission bleeding in the green and red channels when this staining was performed separately (data not shown). We also did not observe cellular autofluorescence in absence of the compounds (data not shown). However, we noticed that the six complexes showed similar cell-staining patterns, undistinguishable when observed in the green and red channels, but with a higher intensity in the green-emission region (Figure 11 and data not shown) according to their spectral profiles. In all cases, the emission was restricted to the cytoplasm, excluded from the nucleus in both cell lines, and more readily visible in perinuclear areas. Accordingly, the localization of luminescent cyclometalated platinum(II) complexes in perinuclear areas of cancer cells with demonstrated cytotoxic activities has been previously described.[7,17]

Complex **2b** showed the brightest cell staining, unlike the other compounds (Table 2), despite its half-exposure time. The greater brightness of this complex also identifies cytoplasmic staining under the cell membrane of both cell lines (yellow arrows in Figure 11), and additionally in protruding filopodia of HeLa cells (orange arrow in Figure 11), which could also indicate an interaction with the cell cytoskeleton elements due to

Table 2. Cytotoxic IC_{50} values [μM] and fluorescence cellular localization, staining patterns, and intensity of complexes **1a**–**c**, **2a**–**c**, and cisplatin.

Complex	A549		HeLa	
	IC_{50}[a]	cellular localization and pattern/ fluorescence intensity[b]	IC_{50}[a]	cellular localization and pattern/fluorescence intensity[b]
1a	NT	cytoplasm, perinuclear; granular/+	NT	cytoplasm, perinuclear; granular/+/−
1b	53.93 ± 3.91	cytoplasm, perinuclear; diffuse/++	55.39 ± 6.69	cytoplasm, perinuclear; diffuse/++
1c	NT	cytoplasm, perinuclear; diffuse/+	NT	cytoplasm, perinuclear; diffuse/+/−
2a	103.5 ± 6.64	cytoplasm, perinuclear; granular/++	74.02 ± 7.33	cytoplasm, perinuclear; granular/++
2b	71.83 ± 7.33	cytoplasm, perinuclear and under plasma membrane; diffuse/++++	61.53 ± 4.04	cytoplasm, perinuclear, under plasma membrane and along filopodia; diffuse/++++
2c	NT	cytoplasm, perinuclear; granular/+	NT	cytoplasm, perinuclear; granular/+
cisplatin	6.45 ± 0.47[c]	−	13.60 ± 0.99	−

[a] IC_{50} values presented as mean ± standard error of the mean of three different experiments. [b] Intensity was classified on a relative scale: −, no staining; +, weak staining; ++, medium staining; +++, strong staining; ++++, very strong staining. [c] As determined in reference [17]. NT = nontoxic: IC_{50} values could not be determined.

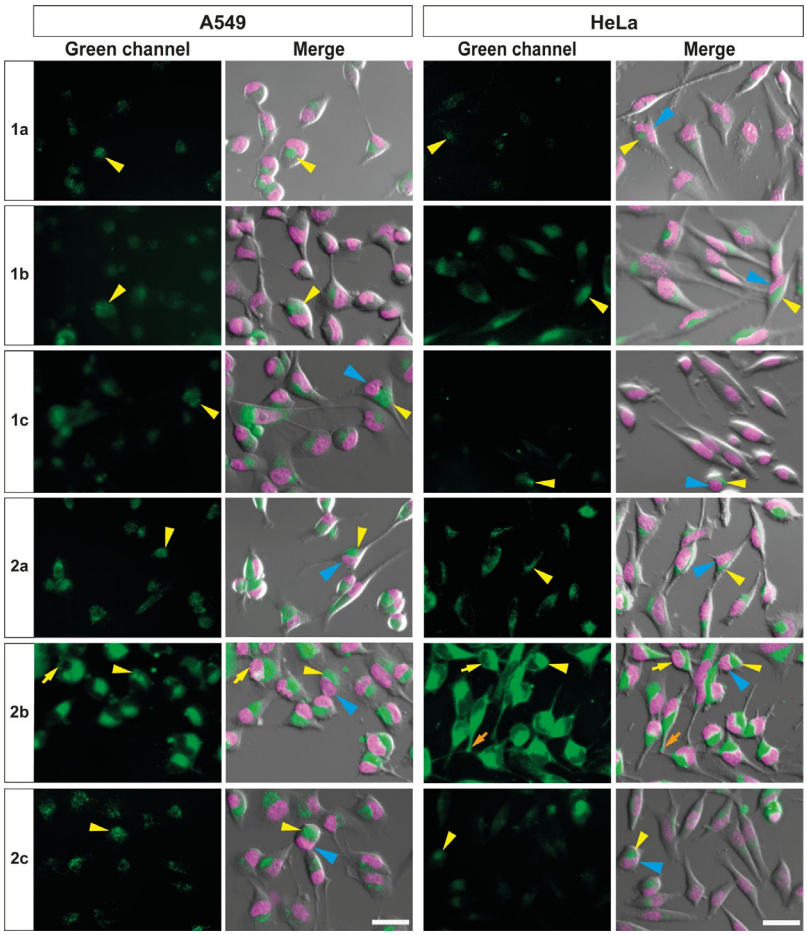

Figure 11. Fluorescence images of A549 and HeLa living cells treated with complexes **1a–c** and **2a–c**. Microscopy images of the green fluorescence emitted by the compounds (left panels) or the overlays of green, magenta (pseudocolor for blue emission of Hoechst, blue arrowheads) and the Nomarski images (right panels). The complexes stain the cytoplasm mainly in perinuclear areas (yellow arrowheads), either in granular (**1a** and **2a**,**c**) or diffuse patterns (**1b**,**c** and **2b**), but do not stain the nuclei (blue arrowheads). Complex **2b** is present under the plasma membrane (yellow arrows) and along the filopodia in HeLa cells (orange arrows). Scale bars: 30 μm.

their similar intracellular distribution.[49] Staining of cytoplasm compartments indicate that cell membranes are permeable to these compounds and demonstrate that the complexes can be traced in living cells by means of emission microscopy. The complexes showed two different staining patterns: either granular (for **1a** and **2a**,**2c**) or diffuse (for **1b**,**c** and **2b**; Figure 11), an effect that could be caused by differential fluorescence-emission enhancement due to interactions with a specific molecular environment in the cytoplasm. Regarding undetectable fluorescent emission from the nucleus, restrained access of complexes to this compartment could cause a limited interaction with DNA and consequently lower DNA damage compared to the cisplatin-related cytotoxic action. Therefore, cytotoxic activity demonstrated by complexes **1b** and **2a**,**b** could be due to alternative molecular mechanisms of action involving molecular targets outside the nucleus, as profusely described for cisplatin and platinum(II) compounds, including defective organization and distribution of the cytoskeleton.[47,50]

Effects of complex 1b on tubulin and microtubule destabilization

In addition to drugs that alter nuclear DNA integrity, mitostatic molecules that bind to tubulins and disrupt microtubule dynamics are widely used as anticancer drugs based on the key role of microtubules in the formation of the mitotic spindle and cytokinesis.[51] Recently, the capability to inhibit tubulin polymerization and degenerate the cytoskeleton network in 518A2 mellanoma cells of a series of organoplatinum(II) complexes has been evaluated in vivo, thus evidencing that some of these complexes act as vascular disrupting agents.[52] Based on the higher cytotoxic activity shown by complex **1b** and its cytoplasmic localization pattern, we explored the capacity of this complex to destabilize tubulin polymerization by immunostaining microtubules with an antitubulin antibody and analyzing the cytoskeletal morphology in A549 and HeLa cells by means of confocal microscopy. Nocodazole was used as a positive control that destabilizes microtubule polymerization,[53] and nontreated cells as a negative control. The exposure of cells to nocodozale-induced microtubule depolymerization in

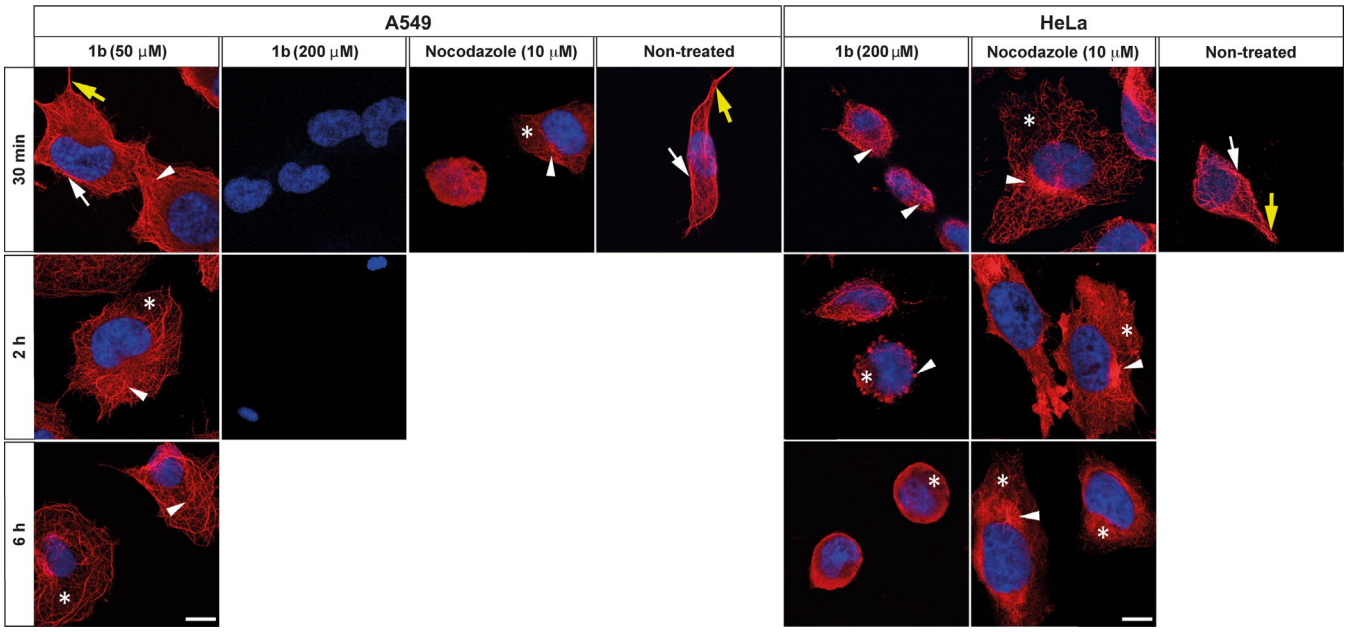

Figure 12. Complex **1 b** destabilizes microtubule polymerization in A549 and HeLa cells. Representative images of double-color confocal microscopy images of cells treated complex **1 b** with nocodazole and nontreated cells. Immunostaining for β-tubulin labels the microtubules in red and 4′,6-diamidino-2-phenylindole (DAPI) stained the nuclei in blue. Nontreated cells show fusiform shapes with the microtubules arranged in parallel under the cell membrane (white arrows) and in protruding filopodia (yellow arrows), whereas nocodazole disorganizes (arrowhead) and depolymerizes (asterisk) the microtubules. The treatment of A549 cells with complex **1 b** at a concentration of 50 μM causes microtubule disorganization with incubation time, and the microtubules disappear after 30 min at a concentration of 200 μM. The effect of **1 b** at 200 μM in HeLa cells is higher than 10 μM nocodazole. Sounded HeLa cells with microtubule disorganization is observed after 30 min (arrowheads), thus reaching high levels of depolymerization after 6 h (asterisk). Scale bars: 10 μm.

both cell lines, although with more efficiency in the A549 cells, led to complete disorganization and depolymerization of the microtubules after 30 min treatment, thus generating rounded cells (Figure 12), as previously reported.[54] Curiously, longer incubation times with nocodazole were required for HeLa cells (up to 2–6 h) to obtain similar effects (Figure 12).[55] Interestingly, complex **1 b** showed effects on the morphology and microtubule organization of A549 cells in a concentration-dependent dose. Thus, tests at 50 μM (IC_{50} value range) caused flattened and rounded morphology, as well as microtubule disorganization, which was readily noticed after 30 min. These are features that progress with longer incubation times (2–6 h) toward advanced microtubule depolymerization. However, when added at 200 μM (four times the IC_{50} value) cells completely lack polymerized microtubules after 30 min, and only picnotic nuclei were present after 2 h (Figure 12, left panels). The tubulin depolymerization activity of complex **1 b** was less pronounced toward HeLa cells and tubulin staining was still visible at 200 μM (around four times the IC_{50} value), worsening after longer exposure times (Figure 12, right panels). These results do not allow us to distinguish whether the effect of complex **1 b** on microtubule destabilization is a unique cause, or even a consequence, of its cytotoxic action; however, the quick action and dynamic similarities of this complex with nocodazole, in addition to its intracellular localization support this hypothesis. Little is known about the effects of cisplatin compounds on the cellular cytoskeleton; nonetheless, there is evidence that supports the ability of cisplatin derivatives to bind, disorganize, and even decrease the expression of cytoskeletal proteins.[50b] Further studies will be needed to find out the biological mechanism of the action of complex **1 b** and related compounds described herein. Recently, a dichloroplatinum(II) complex featuring a 4α-*O*-(2′′,3′′-diaminopropanoyl)podophyllotoxin ligand has been shown to induce cycle arrest in the G_2/M phase and inhibits the formation of microtubules in Hela cells.[56] In a similar line, the inhibition of tubulin polymerization and the degeneration of the cytoskeleton organization in 518A2 melanoma cells have been also found for *N*,*N*-dimethyl-1-(2-aryl)methanamine-κ^2*C*2,*N* cyclometalated [Pt(C^N)Cl(DMSO)] complexes.[52]

Conclusions

We have described the synthesis and properties of two series of 2-(4-substituted)benzothiazolyl cycloplatinated complexes [Pt(R-PBT-κ*C*,*N*)Cl(L)] (R = Br (**1**), Me_2N (**2**)) featuring as auxiliary ligands a labile ligand (DMSO (**a**)) or a water-soluble phosphine (PTA (**b**), TPPTS (**c**)). The low-lying electronic transitions (absorption and emission) in the dimethylamino derivatives **2 a**–**c**, which are expectedly bathochromically shifted relative to **1 a**–**c**, are associated with intraligand charge-transfer transitions (ILCT) from the Me_2N-phenyl donating ring to the acceptor benzothiazole unit [Me_2N-PBT→PBT], whereas these transitions in the bromo-substituted benzothiazole complexes **1 a**–**c** can be described as admixture (LC/MLCT) events. We found that complexes **2 a**,**b** display aggregation-induced luminescence properties related to the occurrence of metal–metal and π···π interactions, which are more enhanced in **2 a** because of the

less bulky DMSO ligand. Furthermore, the optical properties of the Me_2N-PBT complexes, which were examined in detail for **2a**, change on protonation. The interaction of **2a** in aerated acetonitrile with PTSA or in the solid state with hydrogen chloride gas for a short time provokes a reversible and relatively fast protonation of the dimethylamino group, which modifies the nature of the low-energy state from ^{1}ILCT to ^{3}LC/^{3}MLCT (calculations on **2a-H$^+$**) and yields visual changes, with potential in sensing applications. Curiously, we have discovered that prolonged exposure of the yellow solid **2a** to hydrogen chloride gas proceeds with a clean and unexpected subsequent oxidation of the platinum center with concomitant deoxygenation of a coordinated DMSO ligand to afford the red-garnet Pt^{IV}/SMe_2 complex ***mer*-4**, which is converted in solution into ***fac*-4**, as confirmed by X-ray studies. A plausible mechanism that analyzes the involved species by NMR spectroscopy has been proposed.

The analysis of the biological activities of **1** and **2** toward the human-cell lines A549 and HeLa suggests that there is no clear correlation between the substituent Me_2N or Br in the phenyl ring of the cyclometalated PBT group and the cytotoxic activity. Thus, **1b** and **2a**,**b** were more cytotoxic than **1a**,**c** and **2c**, albeit with IC_{50} values higher than cisplatin, and complexes containing PTA (**1b** and **2b**) were the most cytotoxic in spite of their lower solubility in water. Moreover, fluorescence cell imaging indicated a similar biodistribution of both types of complex (**1** and **2**); that is, general cytoplasmic staining was observed in both cell lines, with exclusion from the nucleus and greater visibility in the perinuclear areas. In addition, the capacity of **1b** to destabilize tubulin polymerization in both cell lines provided evidence of a plausible mechanism of its cytotoxic action.

Experimental Section

The experimental details and the crystallographic, photophysical, theoretical, and biological data for the compounds prepared are given in the Supporting Information.

CCDC 1584094, 1584095, 1584096, 1584097, 1584098 contain the supplementary crystallographic data for this paper. These data can be obtained free of charge from The Cambridge Crystallographic Data Centre.

Acknowledgements

This work was supported by the Spanish MINECO (Project CTQ2016-78463-P) and by Fundación Rioja Salud (Gobierno de La Rioja, Spain) to J.G.P. The authors thank CESGA for computer support. S.P.-H. thanks the Sistema Riojano de Innovación (Gobierno de La Rioja, Spain) for a Ph.D. grant and R.L. is grateful for a UR grant.

Conflict of interest

The authors declare no conflict of interest.

Keywords: cell imaging · cytotoxicity · luminescence · platinum · protonation

[1] a) S. Huo, J. Carroll, D. A. K. Vezzu, *Asian J. Org. Chem.* **2015**, *4*, 1210 – 1245; b) V. W.-W. Yam, V. K.-M. Au, S. Y.-L. Leung, *Chem. Rev.* **2015**, *115*, 7589 – 7728; c) J. A. G. Williams, S. Develay, D. L. Rochester, L. Murphy, *Coord. Chem. Rev.* **2008**, *252*, 2596 – 2611; d) J. Kalinowski, V. Fattori, M. Cocchi, J. A. G. Williams, *Coord. Chem. Rev.* **2011**, *255*, 2401 – 2425; e) X. Yang, C. Yao, G. Zhou, *Platinum Met. Rev.* **2013**, *57*, 2 – 16; f) W.-Y. Wong, C.-L. Ho, *Coord. Chem. Rev.* **2009**, *253*, 1709 – 1758; g) V. W.-W. Yam, K. M.-C. Wong, *Chem. Commun.* **2011**, *47*, 11579 – 11592; h) H. Xu, R. Chen, Q. Sun, W. Lai, Q. Su, W. Huang, X. Liu, *Chem. Soc. Rev.* **2014**, *43*, 3259 – 3302; i) W.-Y. Wong, C.-L. Ho, *J. Mater. Chem.* **2009**, *19*, 4457 – 4482; j) H. Xiang, J. Cheng, X. Ma, X. Zhou, J. J. Chruma, *Chem. Soc. Rev.* **2013**, *42*, 6128 – 6185; k) C. L. Ho, W. Y. Wong, *New J. Chem.* **2013**, *37*, 1665 – 1683; l) C. Fan, C. Yang, *Chem. Soc. Rev.* **2014**, *43*, 6439 – 6469; m) C.-L. Ho, H. Li, W.-Y. Wong, *J. Organomet. Chem.* **2014**, *751*, 261 – 285; n) S. Veerasamy, R. Arumugam, T. Pounraj, L. Kuang-Lieh, R. Seenivasan, *J. Photochem. Photobiol. C* **2015**, *23*, 25 – 44.

[2] a) D.-L. Ma, H.-Z. He, K.-H. Leung, D. S.-H. Chan, C.-H. Leung, *Angew. Chem. Int. Ed.* **2013**, *52*, 7666 – 7682; *Angew. Chem.* **2013**, *125*, 7820 – 7837; b) E. Baggaley, J. A. Weinstein, J. A. G. Williams, *Coord. Chem. Rev.* **2012**, *256*, 1762 – 1785; c) M. Mauro, A. Aliprandi, D. Septiadi, N. S. Kehr, L. De Cola, *Chem. Soc. Rev.* **2014**, *43*, 4144 – 4166; d) D.-L. Ma, D. S.-H. Chan, C.-H. Leung, *Acc. Chem. Res.* **2014**, *47*, 3614 – 3631; e) V. Fernández-Moreira, F. L. Thorp-Greenwood, M. P. Coogan, *Chem. Commun.* **2010**, *46*, 186 – 202; f) Q. Zhao, C. Huang, F. Li, *Chem. Soc. Rev.* **2011**, *40*, 2508 – 2524; g) C.-H. Leung, H.-J. Zhong, D. S.-H. Chan, D.-L. Ma, *Coord. Chem. Rev.* **2013**, *257*, 1764 – 1776; h) B. Bertrand, A. Casini, *Dalton Trans.* **2014**, *43*, 4209 – 4219; i) S. Medici, M. Peana, V. M. Nurchi, J. I. Lachowicz, G. Crisponi, M. A. Zoroddu, *Coord. Chem. Rev.* **2015**, *284*, 329 – 350; j) D.-L. Ma, M. Wang, Z. Mao, C. Yang, C.-T. Ng, C.-H. Leung, *Dalton Trans.* **2016**, *45*, 2762 – 2771; k) N. Cutillas, G. S. Yellol, C. de Haro, C. Vicente, V. Rodríguez, J. Ruiz, *Coord. Chem. Rev.* **2013**, *257*, 2784 – 2797; l) I. Omae, *Coord. Chem. Rev.* **2014**, *280*, 84 – 95; m) F. L. Thorp-Greenwood, R. G. Balasingham, M. P. Coogan, *J. Organomet. Chem.* **2012**, *714*, 12 – 21.

[3] a) K. Li, G. S. Ming Tong, Q. Wan, G. Cheng, W.-Y. Tong, W.-H. Ang, W.-L. Kwong, C.-M. Che, *Chem. Sci.* **2016**, *7*, 1653 – 1673; b) A. G. Quiroga, C. Navarro Ranninger, *Coord. Chem. Rev.* **2004**, *248*, 119 – 133; c) W.-P. To, T. Zou, R. W.-Y. Sun, C.-M. Che, *Philos. Trans. R. Soc. A* **2013**, *371*, 20120126; d) A. Zamora, S. A. Pérez, V. Rodríguez, C. Janiak, G. S. Yellol, J. Ruiz, *J. Med. Chem.* **2015**, *58*, 1320 – 1336.

[4] M. Fanelli, M. Formica, V. Fusi, L. Giorgi, M. Micheloni, P. Paoli, *Coord. Chem. Rev.* **2016**, *310*, 41 – 79.

[5] T. Zou, J. Liu, C. T. Lum, C. Ma, R. C.-T. Chan, C.-N. Lok, W.-M. Kwok, C.-M. Che, *Angew. Chem. Int. Ed.* **2014**, *53*, 10119 – 10123; *Angew. Chem.* **2014**, *126*, 10283 – 10287.

[6] a) K. Suntharalingam, A. Łęczkowska, M. A. Furrer, Y. Wu, M. K. Kuimova, B. Therrien, A. J. P. White, R. Vilar, *Chem. Eur. J.* **2012**, *18*, 16277 – 16282; b) D.-L. Ma, C.-M. Che, S.-C. Yan, *J. Am. Chem. Soc.* **2009**, *131*, 1835 – 1846.

[7] R. W.-Y. Sun, A. L.-F. Chow, X.-H. Li, J. J. Yan, S. Sin-Yin Chui, C.-M. Che, *Chem. Sci.* **2011**, *2*, 2109 – 2114.

[8] S. E. Sherman, S. J. Lippard, *Chem. Rev.* **1987**, *87*, 1153 – 1181.

[9] E. R. Jamieson, S. J. Lippard, *Chem. Rev.* **1999**, *99*, 2467 – 2498.

[10] a) S. E. O'Brien, H. L. Browne, T. D. Bradshaw, A. D. Westwell, M. F. G. Stevens, C. A. Laughton, *Org. Biomol. Chem.* **2003**, *1*, 493 – 497; b) B. Mavroidi, M. Sagnou, K. Stamatakis, M. Paravatou-Petsotas, M. Pelecanou, C. Methenitis, *Inorg. Chim. Acta* **2016**, *444*, 63 – 75; c) T. D. Bradshaw, M. F. G. Stevens, A. D. Westwell, *Curr. Med. Chem.* **2001**, *8*, 203 – 210; d) N. H. Nam, P. T. Dung, P. T. Thuong, *Med. Chem.* **2011**, *7*, 127 – 134; e) M. Singh, S. K. Singh, *AntiCancer Agents Med. Chem.* **2014**, *14*, 127 – 146; f) R. S. Keri, M. R. Patil, S. A. Patil, S. Budagumpi, *Eur. J. Med. Chem.* **2015**, *89*, 207 – 251; g) L. Hroch, L. Aitken, O. Benek, M. Dolezal, K. Kuca, F. Gunn-Moore, K. Musilek, *Curr. Med. Chem.* **2015**, *22*, 730 – 747; h) D.-F. Shi, T. D. Bradshaw, S. Wrigley, C. J. McCall, P. Lelieveld, I. Fichtner, M. F. G. Stevens, *J. Med. Chem.* **1996**, *39*, 3375 – 3384.

[11] a) K. G. Desai, K. R. Desai, *Bioorg. Med. Chem.* **2006**, *14*, 8271 – 8279; b) I. Yildiz-Oren, I. Yalcin, E. Aki-Sener, N. Ucarturk, *Eur. J. Med. Chem.* **2004**, *39*, 291 – 298.

[12] C. S. Ra, B. Y. Jung, P. Gyoosoon, *Heterocycles* **2004**, *62*, 793 – 802.

[13] a) W. E. Klunk, Y. Wang, G.-f. Huang, M. L. Debnath, D. P. Holt, C. A. Mathis, *Life Sci.* **2001**, *69*, 1471 – 1484; b) A. Lockhart, L. Ye, D. B. Judd, A. T. Merritt, P. N. Lowe, J. L. Morgenstern, G. Hong, A. D. Gee, J. Brown, *J. Biol. Chem.* **2005**, *280*, 7677 – 7684.

[14] a) Z. Chen, S. Zhang, L. Shen, Z. Zhu, J. Zhang, *New J. Chem.* **2015**, *39*, 1592 – 1596; b) M. Wang, M. Gao, B. H. Mock, K. D. Miller, G. W. Sledge, G. D. Hutchins, Q.-H. Zheng, *Bioorg. Med. Chem.* **2006**, *14*, 8599 – 8607.

[15] a) T. D. Bradshaw, A. D. Westwell, *Curr. Med. Chem.* **2004**, *11*, 1009 – 1021; b) C. O. Leong, M. Suggitt, D. J. Swaine, M. C. Bibby, M. F. G. Stevens, T. D. Bradshaw, *Mol. Cancer Ther.* **2004**, *3*, 1565 – 1575.

[16] a) I. R. Laskar, S.-F. Hsu, T.-M. Chen, *Polyhedron* **2005**, *24*, 881 – 888; b) O. A. Rodionova, M. V. Puzyk, K. P. Balashev, *Opt. Spectrosc.* **2009**, *106*, 523 – 528; c) M. V. Nikolaeva, M. V. Puzyk, *Opt. Spectrosc.* **2013**, *114*, 247 – 250; d) E. A. Katlenok, A. A. Zolotarev, A. Y. Ivanov, S. N. Smirnov, R. I. Baichurin, K. P. Balashev, *Russ J. Coord. Chem.* **2016**, *42*, 178 – 186; e) E. A. Katlenok, A. A. Zolotarev, K. P. Balashev, *Russ. J. Gen. Chem.* **2015**, *85*, 116 – 122.

[17] J. R. Berenguer, J. G. Pichel, N. Giménez, E. Lalinde, M. T. Moreno, S. Piñeiro-Hermida, *Dalton Trans.* **2015**, *44*, 18839 – 18855.

[18] a) R. Lara, E. Lalinde, M. T. Moreno, *Dalton Trans.* **2017**, *46*, 4628 – 4641; b) N. Giménez, R. Lara, M. T. Moreno, E. Lalinde, *Chem. Eur. J.* **2017**, *23*, 5758 – 5771.

[19] a) G. Süss-Fink, *Dalton Trans.* **2010**, *39*, 1673 – 1688; b) S. Parveen, M. Hanif, S. Movassaghi, M. P. Sullivan, M. Kubanik, M. A. Shaheen, T. Söhnel, S. M. F. Jamieson, C. G. Hartinger, *Eur. J. Inorg. Chem.* **2017**, 1721 – 1727; c) A. R. Burgoyne, C. H. Kaschula, M. I. Parker, G. S. Smith, *Eur. J. Inorg. Chem.* **2016**, 1267 – 1273; d) R. Pettinari, A. Petrini, F. Marchetti, C. Pettinari, T. Riedel, B. Therrien, P. J. Dyson, *Eur. J. Inorg. Chem.* **2017**, 1800 – 1806; e) J. Palmucci, F. Marchetti, R. Pettinari, C. Pettinari, R. Scopelliti, T. Riedel, B. Therrien, A. Galindo, P. J. Dyson, *Inorg. Chem.* **2016**, *55*, 11770 – 11781; f) S. Seršen, J. Kljun, K. Kryeziu, R. Panchuk, B. Alte, W. Körner, P. Heffeter, W. Berger, I. Turel, *J. Med. Chem.* **2015**, *58*, 3984 – 3996; g) L. Tabrizi, H. Chiniforoshan, *J. Organomet. Chem.* **2016**, *822*, 211 – 220; h) Z. Wang, H. Qian, S.-M. Yiu, J. Sun, G. Zhu, *J. Inorg. Biochem.* **2014**, *131*, 47 – 55; i) W. H. Ang, A. Casini, G. Sava, P. J. Dyson, *J. Organomet. Chem.* **2011**, *696*, 989 – 998.

[20] a) E. Guerrero, S. Miranda, S. Lüttenberg, N. Fröhlich, J.-M. Koenen, F. Mohr, E. Cerrada, M. Laguna, A. Mendía, *Inorg. Chem.* **2013**, *52*, 6635 – 6647; b) C. Mügge, C. Rothenburger, A. Beyer, H. Gorls, C. Gabbiani, A. Casini, E. Michelucci, I. Landini, S. Nobili, E. Mini, L. Messori, W. Weigand, *Dalton Trans.* **2011**, *40*, 2006 – 2016; c) J. Ruiz, V. Rodríguez, N. Cutillas, A. Espinosa, M. J. Hannon, *J. Inorg. Biochem.* **2011**, *105*, 525 – 531; d) P. Chellan, K. M. Land, A. Shokar, A. Au, S. H. An, C. M. Clavel, P. J. Dyson, C. D. Kock, P. J. Smith, K. Chibale, G. S. Smith, *Organometallics* **2012**, *31*, 5791 – 5799; e) P. Bergamini, V. Bertolasi, L. Marvelli, A. Canella, R. Gavioli, N. Mantovani, S. Mañas, A. Romerosa, *Inorg. Chem.* **2007**, *46*, 4267 – 4276; f) A. Romerosa, P. Bergamini, V. Bertolasi, A. Canella, M. Cattabriga, R. Gavioli, S. Mañas, N. Mantovani, L. Pellacani, *Inorg. Chem.* **2004**, *43*, 905 – 913.

[21] a) E. García-Moreno, A. Tomas, E. Atrián-Blasco, S. Gascón, E. Romanos, M. J. Rodríguez-Yoldi, E. Cerrada, M. Laguna, *Dalton Trans.* **2016**, *45*, 2462 – 2475; b) E. García-Moreno, S. Gascón, E. Atrián-Blasco, M. J. Rodriguez-Yoldi, E. Cerrada, M. Laguna, *Eur. J. Med. Chem.* **2014**, *79*, 164 – 172; c) E. Atrián-Blasco, S. Gascón, M. J. Rodríguez-Yoldi, M. Laguna, E. Cerrada, *Eur. J. Inorg. Chem.* **2016**, 2791 – 2803; d) R. Gavara, E. Aguiló, J. Schur, J. Llorca, I. Ott, L. Rodríguez, *Inorg. Chim. Acta* **2016**, *446*, 189 – 197; e) E. García-Moreno, S. Gascón, M. J. Rodriguez-Yoldi, E. Cerrada, M. Laguna, *Organometallics* **2013**, *32*, 3710 – 3720; f) J. Arcau, V. Andermark, E. Aguilo, A. Gandioso, A. Moro, M. Cetina, J. C. Lima, K. Rissanen, I. Ott, L. Rodriguez, *Dalton Trans.* **2014**, *43*, 4426 – 4436; g) B. T. Elie, C. Levine, I. Ubarretxena-Belandia, A. Varela-Ramírez, R. J. Aguilera, R. Ovalle, M. Contel, *Eur. J. Inorg. Chem.* **2009**, 3421 – 3430; h) S. Wan, W. Lu, *Angew. Chem. Int. Ed.* **2017**, *56*, 1784 – 1788; *Angew. Chem.* **2017**, *129*, 1810 – 1814; i) E. Vergara, A. Casini, F. Sorrentino, O. Zava, E. Cerrada, M. P. Rigobello, A. Bindoli, M. Laguna, P. J. Dyson, *ChemMedChem* **2010**, *5*, 96 – 102; j) E. Vergara, E. Cerrada, C. Clavel, A. Casini, M. Laguna, *Dalton Trans.* **2011**, *40*, 10927 – 10935.

[22] a) P. S. Pregosin, F. Wombacher, A. Albinati, F. Lianza, *J. Organomet. Chem.* **1991**, *418*, 249 – 267; b) J. Forniés, V. Sicilia, C. Larraz, J. A. Camerano, A. Martín, J. M. Casas, A. C. Tsipis, *Organometallics* **2010**, *29*, 1396 – 1405.

[23] D. J. Mabbott, B. E. Mann, P. M. Maitlis, *J. Chem. Soc. Dalton Trans.* **1977**, 294 – 299.

[24] V. Sicilia, S. Fuertes, A. Martín, A. Palacios, *Organometallics* **2013**, *32*, 4092 – 4102.

[25] a) A. R. Esmaeilbeig, M. G. Haghighi, S. Nikahd, S. Hashemi, M. Mosarezaee, M. Rashidi, S. M. Nabavizadeh, *J. Organomet. Chem.* **2014**, *755*, 93 – 100; b) M. G. Haghighi, M. Rashidi, S. M. Nabavizadeh, S. Jamali, R. J. Puddephatt, *Dalton Trans.* **2010**, *39*, 11396 – 11402.

[26] a) S. A. De Pascali, P. Papadia, A. Ciccarese, C. Pacifico, F. P. Fanizzi, *Eur. J. Inorg. Chem.* **2005**, 788 – 796; b) D. Belli Dell Amico, L. Dalla Via, A. N. García-Argáez, L. Labella, F. Marchetti, S. Samaritani, *Polyhedron* **2015**, *85*, 685 – 689; c) C. Mügge, R. Liu, H. Gorls, C. Gabbiani, E. Michelucci, N. Rudiger, J. H. Clement, L. Messori, W. Weigand, *Dalton Trans.* **2014**, *43*, 3072 – 3086.

[27] a) S.-W. Lai, Q. K. W. Chan, J. Han, Y.-G. Zhi, N. Zhu, C.-M. Che, *Organometallics* **2009**, *28*, 34 – 37; b) V. V. Sivchik, A. I. Solomatina, Y.-T. Chen, A. J. Karttunen, S. P. Tunik, P.-T. Chou, I. O. Koshevoy, *Angew. Chem. Int. Ed.* **2015**, *54*, 14057 – 14060; *Angew. Chem.* **2015**, *127*, 14263 – 14266.

[28] a) A. Díez, J. Forniés, A. García, E. Lalinde, M. T. Moreno, *Inorg. Chem.* **2005**, *44*, 2443 – 2453; b) N. Godbert, T. Pugliese, I. Aiello, A. Bellusci, A. Crispini, M. Ghedini, *Eur. J. Inorg. Chem.* **2007**, 5105 – 5111; c) N. Cutillas, A. Martínez, G. S. Yellol, V. Rodríguez, A. Zamora, M. Pedreño, A. Donaire, C. Janiak, J. Ruiz, *Inorg. Chem.* **2013**, *52*, 13529 – 13535; d) A. Zucca, L. Maidich, V. Carta, G. L. Petretto, S. Stoccoro, M. Agostina Cinellu, M. I. Pilo, G. J. Clarkson, *Eur. J. Inorg. Chem.* **2014**, 2278 – 2287.

[29] S. E. McLain, A. K. Soper, A. Luzar, *J. Chem. Phys.* **2006**, *124*, 074502.

[30] D. E. Janzen, L. F. Mehne, D. G. VanDerveer, G. J. Grant, *Inorg. Chem.* **2005**, *44*, 8182 – 8184.

[31] a) J. Braddock-Wilking, S. Acharya, N. P. Rath, *Polyhedron* **2014**, *79*, 16 – 28; b) D. A. Krogstad, J. Cho, A. J. DeBoer, J. A. Klitzke, W. R. Sanow, H. A. Williams, J. A. Halfen, *Inorg. Chim. Acta* **2006**, *359*, 136 – 148; c) D. Dolfen, K. Schottler, S.-M. Valiahdi, M. A. Jakupec, B. K. Keppler, E. R. T. Tiekink, F. Mohr, *J. Inorg. Biochem.* **2008**, *102*, 2067 – 2071.

[32] a) Y. Zhang, J. Clavadetscher, M. Bachmann, O. Blacque, K. Venkatesan, *Inorg. Chem.* **2014**, *53*, 756 – 771; b) J. R. Berenguer, E. Lalinde, A. Martín, M. T. Moreno, S. Sánchez, H. R. Shahsavari, *Inorg. Chem.* **2016**, *55*, 7866 – 7878; c) J. R. Berenguer, A. Díez, E. Lalinde, M. T. Moreno, S. Ruiz, S. Sánchez, *Organometallics* **2011**, *30*, 5776 – 5792.

[33] J. R. Berenguer, E. Lalinde, M. T. Moreno, S. Sánchez, J. Torroba, *Inorg. Chem.* **2012**, *51*, 11665 – 11679.

[34] a) S. Y.-L. Leung, S. Evariste, C. Lescop, M. Hissler, V. W.-W. Yam, *Chem. Sci.* **2017**, *8*, 4264 – 4273; b) V. V. Sivchik, E. V. Grachova, A. S. Melnikov, S. N. Smirnov, A. Y. Ivanov, P. Hirva, S. P. Tunik, I. O. Koshevoy, *Inorg. Chem.* **2016**, *55*, 3351 – 3363.

[35] A. Díez, J. Forniés, S. Fuertes, C. Larraz, J. A. López, E. Lalinde, A. Martín, M. T. Moreno, V. Sicilia, *Organometallics* **2009**, *28*, 1705 – 1718.

[36] a) D. Escudero, *Acc. Chem. Res.* **2016**, *49*, 1816 – 1824; b) J. Zhao, F. Dang, Z. Feng, B. Liu, X. Yang, Y. Wu, G. Zhou, Z. Wu, W.-Y. Wong, *Chem. Commun.* **2017**, *53*, 7581 – 7584; c) Z. R. Grabowski, K. Rotkiewicz, W. Rettig, *Chem. Rev.* **2003**, *103*, 3899 – 4032.

[37] Y. Chi, P. T. Chou, *Chem. Soc. Rev.* **2010**, *39*, 638 – 655.

[38] W. Wu, W. Wu, S. Ji, H. Guo, J. Zhao, *Eur. J. Inorg. Chem.* **2010**, 4470 – 4482.

[39] a) M. R. R. Prabhath, J. Romanova, R. J. Curry, S. R. P. Silva, P. D. Jarowski, *Angew. Chem. Int. Ed.* **2015**, *54*, 7949 – 7953; *Angew. Chem.* **2015**, *127*, 8060 – 8064; b) S. C. F. Kui, P. K. Chow, G. S. M. Tong, S.-L. Lai, G. Cheng, C.-C. Kwok, K.-H. Low, M. Y. Ko, C.-M. Che, *Chem. Eur. J.* **2013**, *19*, 69 – 73; c) P. Pinter, R. Pittkowski, J. Soellner, T. Strassner, *Chem. Eur. J.* **2017**, *23*, 14173 – 14176.

[40] J. R. Berenguer, E. Lalinde, J. Torroba, *Inorg. Chem.* **2007**, *46*, 9919 – 9930.

[41] a) V. Y. Kukushkin, *Coord. Chem. Rev.* **1995**, *139*, 375 – 407; b) X. Wang, L. K. Woo, *J. Org. Chem.* **1998**, *63*, 356 – 360.

[42] C. S. Mota, M. G. Rivas, C. D. Brondino, I. Moura, J. J. G. Moura, *J. Biol. Inorg. Chem.* **2011**, *16*, 1255 – 1268.

[43] L. Alexandrova, O. G. D'Yachenko, G. M. Kazankov, V. A. Polyakov, P. V. Samuleev, E. Sansores, A. D. Ryabov, *J. Am. Chem. Soc.* **2000**, *122*, 5189 – 5200.

[44] a) J. A. Labinger, *Chem. Rev.* **2017**, *117*, 8483 – 8496; b) M. Lersch, M. Tilset, *Chem. Rev.* **2005**, *105*, 2471 – 2526; c) R. J. Puddephatt, *Coord. Chem. Rev.* **2001**, *219 – 221*, 157 – 185.

[45] a) R. W.-Y. Sun, C.-N. Lok, T. T.-H. Fong, C. K.-L. Li, Z. F. Yang, T. Zou, A. F.-M. Siu, C.-M. Che, *Chem. Sci.* **2013**, *4*, 1979 – 1988; b) S. Dhar, W. L. Daniel, D. A. Giljohann, C. A. Mirkin, S. J. Lippard, *J. Am. Chem. Soc.* **2009**, *131*, 14652 – 14653.

[46] a) L. M. Levasseur, H. K. Slocum, Y. M. Rustum, W. R. Greco, *Cancer Res.* **1998**, *58*, 5749 – 5761; b) S. B. Hassan, E. Jonsson, R. Larsson, M. O. Karlsson, *J. Pharmacol. Exp. Ther.* **2001**, *299*, 1140 – 1147.

[47] S. Dasari, P. Bernard Tchounwou, *Eur. J. Pharmacol.* **2014**, *740*, 364 – 378.

[48] R. M. Martin, H. Leonhardt, M. C. Cardoso, *Cytometry Part A* **2005**, *67A*, 45 – 52.

[49] O. C. Rodriguez, A. W. Schaefer, C. A. Mandato, P. Forscher, W. M. Bement, C. M. Waterman-Storer, *Nat. Cell Biol.* **2003**, *5*, 599 – 609.

[50] a) T. C. Johnstone, K. Suntharalingam, S. J. Lippard, *Chem. Rev.* **2016**, *116*, 3436 – 3486; b) D.-W. Shen, X.-J. Liang, M. A. Gawinowicz, M. M. Gottesman, *Mol. Pharmacol.* **2004**, *66*, 1265 – 1274.

[51] a) K. H. Downing, *Ann. Rev. Cell Dev. Biol.* **2000**, *16*, 89 – 111; b) A. Jordan, J. A. Hadfield, N. J. Lawrence, A. T. McGowyn, *Med. Res. Rev.* **1998**, *18*, 259 – 296.

[52] A. Zamora, S. A. Pérez, M. Rothemund, V. Rodríguez, R. Schobert, C. Janiak, J. Ruiz, *Chem. Eur. J.* **2017**, *23*, 5614 – 5625.

[53] L. U. Cassimeris, P. Wadsworth, E. D. Salmon, *J. Cell Biol.* **1986**, *102*, 2023 – 2032.

[54] D. L. Sackett, L. Ozbun, E. Zudaire, L. Wessner, J. M. Chirgwin, F. Cuttitta, A. Martínez, *Endocrinology* **2008**, *149*, 2888 – 2898.

[55] Y.-C. Chang, P. Nalbant, J. Birkenfeld, Z.-F. Chang, G. M. Bokoch, *Mol. Biol. Cell* **2008**, *19*, 2147 – 2153.

[56] X. Liu, L.-L. Zhang, X.-H. Xu, L. Hui, J.-B. Zhang, S.-W. Chen, *Bioorg. Med. Chem. Lett.* **2013**, *23*, 3780 – 3784.

Manuscript received: November 6, 2017
Accepted manuscript online: December 8, 2017
Version of record online: January 25, 2018